Neural Network Interaction Potentials for *para*-Hydrogen with Flexible Molecules

Laura Durán Caballero,[1] Christoph Schran,[1, a)] Fabien Brieuc,[1, b)] and Dominik Marx[1]
Lehrstuhl für Theoretische Chemie, Ruhr-Universität Bochum, 44780 Bochum, Germany

(*Electronic mail: laura.duran-caballero@rub.de)

(Dated: 22 June 2022)

The study of molecular impurities in *para*-hydrogen (pH_2) clusters is key to push forward our understanding of intra- and intermolecular interactions including their impact on the superfluid response of this bosonic quantum solvent. This includes tagging with only one or very few pH_2, the microsolvation regime for intermediate particle numbers, and matrix isolation with many solvent molecules. However, the fundamental coupling between the bosonic pH_2 environment and the (ro-)vibrational motion of molecular impurities remains poorly understood. Quantum simulations can in principle provide the necessary atomistic insight, but they require very accurate descriptions of the involved interactions. Here, we present a data-driven approach for the generation of *impurity*$\cdots pH_2$ interaction potentials based on machine learning techniques which retain the full flexibility of the dopant species. We employ the well-established adiabatic hindered rotor (AHR) averaging technique to include the impact of the nuclear spin statistics on the symmetry-allowed rotational quantum numbers of pH_2. Embedding this averaging procedure within the high-dimensional neural network potential (NNP) framework enables the generation of highly-accurate AHR-averaged NNPs at coupled cluster accuracy, namely CCSD(T*)-F12a/aVTZcp, in an automated manner. We apply this methodology to the water and protonated water molecules, as representative cases for quasi-rigid and highly-flexible molecules respectively, and obtain AHR-averaged NNPs that reliably describe the corresponding $H_2O\cdots pH_2$ and $H_3O^+\cdots pH_2$ interactions. Using path integral simulations we show for the hydronium cation, H_3O^+, that umbrella-like tunneling inversion has a strong impact on the first and second pH_2 microsolvation shells. The automated and data-driven nature of our protocol opens the door to the study of bosonic pH_2 quantum solvation for a wide range of embedded impurities.

I. INTRODUCTION

It has been known for a long time that ^{4}He is superfluid at temperatures below 2.17 K.[1,2] In the search for other substances that could be superfluid, *para*-hydrogen (pH_2) — a zero-spin boson characterized by even values of the rotational quantum number — was considered very early to be a suitable candidate,[3] yet experimental evidence of superfluid behavior of OCS-doped pH_2 clusters embedded in helium nanodroplets was only reported[4] in 2000 although it has been predicted computationally for pure pH_2 clusters roughly ten years earlier.[5] Note that a different interpretation of the experimental signatures has been advanced in 2019 based on computational evidence for the valence-isoelectronic CO_2 dopant — culminating in the conclusion that CO_2-doped pH_2 clusters embedded within ^{4}He clusters feature minimal superfluid response but instead phase-separate and form a nonsuperfluid $CO_2(pH_2)_N$ core therein.[6] Independently from this discussion, the bosonic nature of pH_2 together with its low mass make it a perfect candidate to undergo a superfluid transition. While bulk pH_2 remains solid even at ultra-low temperatures due to the relatively strong intermolecular interactions,[7] pure pH_2 clusters of specific size were predicted to feature manifestations of superfluidity by various quantum simulations.[5,8–17] However, experimental verification of these effects can only be indirectly achieved and, additionally, might be challenging to correctly interpret. But given the routine use of pH_2 in both, matrix isolation spectroscopy[18,19] and vibrational photodissociation spectroscopy using messenger tagging[20–22] it is necessary to advance our microscopic understanding of the intermolecular interactions between pH_2 and molecular impurities as well as the possible coupling to superfluidity using accurate and predictive calculations.

In order to bring light into these questions, quantum simulation techniques are crucial to provide atomistic insights as has been demonstrated since decades. Already in 1991, pioneering Path Integral Monte Carlo (PIMC) simulations of small pH_2 clusters predicted superfluid behavior for 13 and 18 molecules below 2 K.[5] Although several studies on pH_2,[5,8–17] *ortho*-deuterium,[10,23,24] and mixed[25–27] clusters have been performed since then, theoretical studies regarding molecular impurities in pH_2 have mainly been limited to small neutral molecules including, among others, OCS,[28] CO_2,[6,29,30] CO,[31] CH_4,[32] SO_2[33] and H_2O[34] as reviewed in Ref. 15. Importantly, all these studies have been performed while freezing the nuclear skeleton of the molecular impurities, thus treating them as (quantum) rigid rotors embedded in pH_2 clusters while neglecting the vibrational degrees of freedom.[35] Simulating non-atomic impurities in bosonic environments as rigid bodies is expected to be an almost perfect approximation for the plethora of quasi-rigid molecules such as OCS, CO_2, CH_4 or H_2O, but this assumption might introduce severe artifacts when investigating non-covalently bound molecular complexes[36,37] and even more so for floppy molecules[38–40] all belonging to the family of non-rigid systems.

To date only very few simulation techniques exist to go beyond the rigid rotor treatment of molecular impurities in su-

[a)]Present address: Yusuf Hamied Department of Chemistry, University of Cambridge, Cambridge, CB2 1EW, UK
[b)]Present address: Laboratoire Matière en Conditions Extrêmes, Université Paris-Saclay, CEA, DAM, DIF, 91297 Arpajon, France

perfluid quantum solvents at ultra-low but finite temperatures. The hybrid path integral molecular dynamics/bosonic path integral Monte Carlo (HPIMD/MC) technique[36,37] developed in our group is one of the few examples, as recently reviewed in Ref. 41. The combination of both approaches makes it possible to run converged path integral simulations at ultra-low temperatures including the bosonic character of the quantum solvent (via bosonic exchange PIMC sampling) while keeping the flexibility of the dopant molecule (via PIMD propagation). This methodology has so far been used to study reactive HCl$\cdots$water clusters in superfluid helium nanodroplets[36,37] as well as protonated methane[39,40] and protonated water clusters[42] microsolvated by ^{4}He atoms.

Unfortunately, the application of this finite-temperature methodology to pH$_2$ is not straightforward, as accounting for bosonic exchange requires treating the quantum solvent as identical point-like particles using present-day simulation techniques to sample symmetrized path integrals in order to establish Bose-Einstein statistics. Traditionally, an isotropic spherical average over the orientation of the two-site H$_2$ molecule has been performed[28,43–47] to generate a spherical single-site interaction potential for pH$_2$. However, it has been shown later that a non-negligible error is made when using this approach to describe the interaction potential between pH$_2$ and molecular impurities, especially for strongly interacting and anisotropic systems, such as the water molecule.[48] The so-called 'adiabatic hindered rotor' (AHR) approximation[48,49] has been devised to overcome this problem by effectively including the anisotropy of the interaction potential into the averaging procedure. This allows one to treat pH$_2$ in bosonic quantum simulations as if it were a spherical point particle.

Although reliable and even highly accurate pair potentials for the description of the pH$_2\cdots p$H$_2$ interaction are available in the literature, such as the semiempirical Silvera-Goldman pair potential[50] and electronic-structure-based two- and three-body potentials,[51,52] it remains difficult to obtain accurate interaction potentials between dopant molecules and pH$_2$ despite much progress.[33,48,49,53,54] The generation of such potentials using physically motivated functional forms is usually very challenging and a time-consuming task in part because the functions used are rarely transferable from one system to another. Machine learning techniques have been shown to be a promising alternative[57]**?** for the current task for which most steps of the development can be easily automated,[42] and transferred to a new system while using basically converged coupled cluster accuracy at the level of the reference calculations.

In this work, we introduce a general methodology to generate highly accurate AHR-averaged potentials to describe the interaction between a molecular impurity and pH$_2$ in the framework of high-dimensional neural network potentials (NNPs).[55–57] Our data-driven approach consists of a 3-step process: First an all-atom NNP is generated for the interaction potential between H$_2$ and the dopant molecule, where H$_2$ is treated as a diatomic molecule. Next the AHR-average is performed using this all-atom NNP in an automated procedure to generate the effective interactions of point-like pH$_2$ with the impurity. Finally, a NNP representation of the *dopant*$\cdots p$H$_2$ interaction potential is obtained based on this effective single-site treatment of pH$_2$. We demonstrate the capabilities of this data-driven procedure for the interaction potential of pH$_2$ with water, for which existing AHR potentials are available for reference[48] where H$_2$O has been described as a rigid body. We also apply it to the distinctly non-rigid and strongly interacting hydronium cation (H$_3$O$^+$), where the inclusion of the full flexibility of the molecular dopant is crucial as will be demonstrated. Importantly, our AHR-averaged NNP interaction potential allows one to include the (ro-vibrational) flexibility of these two impurities at the level of bosonic HPIMD/MC quantum simulations. Overall, this work opens up the possibility for the computational study of utmost floppy and even reactive impurities under bosonic pH$_2$ solvation to shed light on the coupling of superfluid behavior and intermolecular interactions as disclosed previously for the highly fluxional protonated methane molecule (CH_5^+) interacting with bosonic helium.[39,40]

II. METHODOLOGY

A key aspect of most computational approaches for investigating molecular impurities in bosonic quantum solvents is to describe the full system as the sum of *solute*$\cdots$*solvent*, *solvent*$\cdots$*solvent* and possibly intra-solute interactions which allows the simulations to be computationally efficient. Performing such simulations using pH$_2$ as the quantum solvent requires the treatment of the pH$_2$ molecules as spherical point-like particles to practically include bosonic exchange. In order to generate an interaction potential between the molecular impurity and the point-like pH$_2$, it is necessary to use a suitable averaging procedure over the orientation of the pH$_2$ molecule as already alluded to in the introduction. It has been shown that the AHR approximation[48,49,53,54] can be used to perform such an anisotropic average including the allowed rotational levels to obtain a reduced-dimension interaction potential where pH$_2$ is an effective spherical point particle. Here, this well-established approach will be combined with machine learning methodology in order to produce highly-accurate *solute*$\cdots$*solvent* interaction potentials of fully flexible and possibly reactive molecular dopants with a point-like pH$_2$ molecule.

Our data-driven process consists of three steps. First, an all-atom NNP for the interaction potential between H$_2$ and the impurity of interest is generated, where the rotational degrees of freedom of the H$_2$ molecule are treated explicitly while its bond length is fixed at its vibrational average in the ground state (0.7668 Å).[58] The all-atom NNP is fitted to highly-accurate coupled cluster electronic structure calculations. Secondly, this all-atom NNP is used to most efficiently perform the AHR averaging using that interim interaction potential in order to reduce the pH$_2$ molecule to an effective spherical point particle and thus to a single interaction site. Finally, a single-site NNP is generated for the point-like particle representation of the pH$_2$ interaction potential, in which the obtained AHR-averaged NNP energies are used as reference data to fit the final AHR-averaged (single-site) NNP. A

schematic representation of this 3-step process can be found in Figure 1.

Our machine learning approach builds on the concepts of high-dimensional neural network potentials (NNPs) combined with atom-centered symmetry functions[59] as developed by Behler and coworkers.[55–57,59] This methodology first transforms the atomic coordinates using a set of symmetry functions[59] into suitable input for atomic neural networks. These atomic neural networks output atomic energy contributions such that the total high-dimensional NNP interaction energy is the sum of the atomic contributions obtained by the atomic NNs.

The generation of such interaction NNPs can be automated and tuned to efficiently select the configurations for optimal training of the NNP so that the number of expensive reference electronic structure calculations is minimized, as introduced and described in detail in Ref. 42 for the case of helium interacting with protonated water clusters. This active-learning procedure is based on two strategies in order to efficiently select the structures that are added to the reference dataset, by using the flexibility of neural networks to our advantage. On one side, this flexibility can be used to detect underrepresented regions of the configuration space. This is achieved by comparing two differently trained NNPs and identifying the configurations that feature the largest disagreement. On the other side, extrapolation of the NNP can be easily detected so that configurations outside of the sampled configuration space can be added to the training set, thus expanding its boundaries. The all-atom interaction NNP is generated using our automated procedure,[42] but adapted from the single-site He atom to the two-site H_2 molecule in order to include the additional degrees of freedom coming from the orientation of the diatomic molecule around its center of mass. Furthermore, we now make use of the advantages of committee approaches[60] to achieve an improved accuracy of our new interaction NNPs. Once the dataset is generated, different NNPs are fitted to form a committee NNP, where the prediction of the model is given by the average over the committee members. This approach is widely used in the neural network community as it improves the accuracy of the models at not much additional computational cost and also since it provides a generalization of error estimates. For more background and details on this approach we refer the interested reader to Ref. 60.

Once the all-atom NNP for the interaction of H_2 with a specific molecular impurity is generated, the AHR approximation[48,49,53,54] is used to reduce the dimensionality of the pH_2 molecule while incorporating the required nuclear spin statistics by considering only the even rotational levels in the rotational average. The AHR approximation is based on the assumption that the H_2 rotation is much faster than the motion of the other degrees of freedom, and can therefore be adiabatically separated and averaged out by considering only the allowed rotational states, i.e. symmetric w.r.t permutations of the two protons for pH_2. The adiabatic Schrödinger equation

$$\left(\hat{T}_{H_2} + \frac{\hbar^2}{2\mu R^2}\hat{j}^2_{H_2} + V(R,\theta,\phi,\theta',\phi')\right)\psi(\theta',\phi';R,\theta,\phi) = V^{\mathrm{AHR}}(R,\theta,\phi)\;\psi(\theta',\phi';R,\theta,\phi)\;, \tag{1}$$

is solved, where the lowest eigenvalue is the AHR-averaged potential $V^{\mathrm{AHR}}(R,\theta,\phi)$ at a given position of the pH_2 molecule, $V(R,\theta,\phi,\theta',\phi')$ is the all-atom interaction potential (obtained here from the all-atom NNP), $\hat{T}_{H_2}$ is the kinetic energy operator of H_2, $\hat{j}^2_{H_2}$ is the angular momentum operator of H_2 and μ is the reduced mass of the *impurity*$\cdots pH_2$ pair; see the middle panel of Figure 1 for the definition of the required coordinates $(R,\theta,\phi,\theta',\phi')$. To solve this equation, spherical harmonics are used as basis functions to represent the rotational eigenstates

$$\psi(\theta',\phi';R,\theta,\phi) = \sum_{l,m} C_l^m(R,\theta,\phi) Y_l^m(\theta',\phi') \tag{2}$$

but considering only even values of l together with the corresponding set of m quantum numbers in the summation as required for pH_2; note that including only the spherically symmetric $l = 0$ term in that sum yields the isotropic spherical quantum average of the interaction potential.

The contribution coming from the H_2 kinetic energy and angular momentum operators to the AHR-averaged potential are easily obtained. On the contrary, the evaluation of the contribution coming from the potential energy term is more complicated, as it requires the computation of the following matrix elements

$$\langle Y_{l'}^{m'}|V(R,\theta,\phi,\theta',\phi')|Y_l^m\rangle = \int_0^\pi d\theta' \sin\theta' \int_0^{2\pi} d\phi'\, Y_{l'}^{m'}(\theta',\phi')\, V(R,\theta,\phi,\theta',\phi')\, Y_l^m(\theta',\phi')\,. \tag{3}$$

These two integrals are computed numerically using Gauss-Legendre and Gauss-Chebyshev quadratures for θ' and ϕ', respectively, while using the all-atom NNP.

When performing the AHR average, we consider the coordinate system employed in previous pioneering work.[48] It is defined such that the origin of coordinates is at the center of mass of the impurity, with its principal rotational axis aligned with the z axis. Then, an atom not belonging to the rotational axis is placed on the xz plane. A second coordinate system is used for H_2, denoted here with $'$, which has the same orientation as the impurity's coordinate system but its origin at the center of mass of the H_2 molecule. Here, R, θ and ϕ define the position of the center of mass of the pH_2 with respect to the origin of coordinates of the impurity's coordinate system, whereas θ' and ϕ' define the orientation of the pH_2 molecule with respect to its center of mass. This definition of the coordinate system for water is shown in the central panel of Figure 1. For more details on the AHR-averaging procedure, we refer the interested reader to Refs. 48,49,53,54.

The third and last step in our data-driven protocol is to train a second NNP for the system where pH_2 is treated as a point-like particle. This AHR-averaged NNP is generated using the same automated procedure as in the generation of the all-atom NNP introduced above, with the difference that now the AHR-averaged interaction energy $V^{\mathrm{AHR}}(R,\theta,\phi)$ from the solution of the adiabatic Schrödinger equation Eq. (1) is used

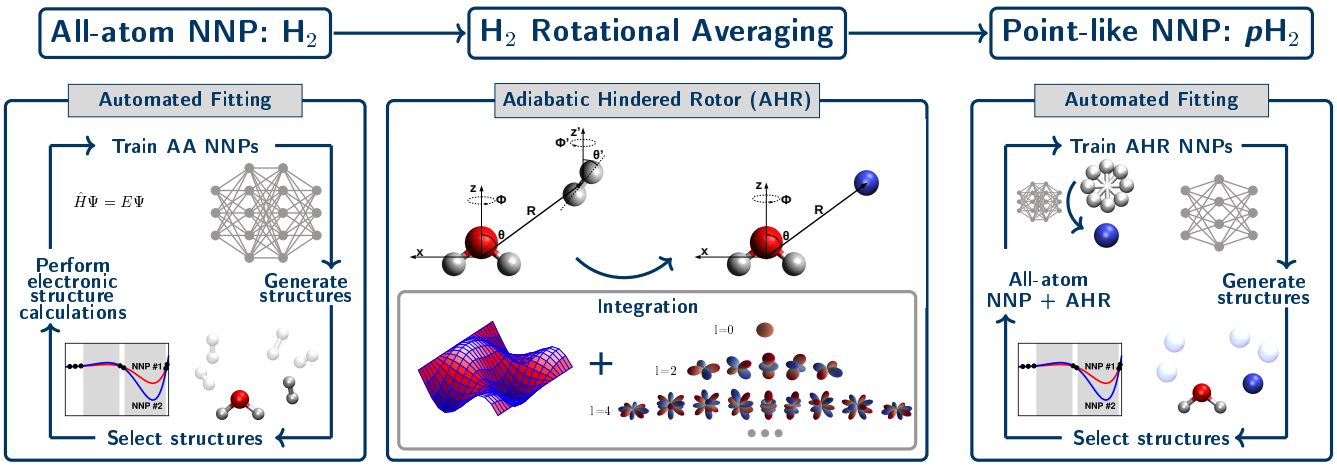

FIG. 1. Schematic representation of the data-driven 3-step development process for generating all-atom H_2 and single-site AHR-averaged pH_2 neural network interaction potentials. The left panel shows the generation of the interim all-atom interaction NNP via an automated active learning procedure where the diatomic nature of the H_2 molecule is explicitly considered. Then, that final all-atom NNP is used to perform the adiabatic hindered rotor (AHR) averaging (middle panel). In this step we reduce the dimensionality of the pH_2 molecule from all-atom to a point-like particle, while imposing the required nuclear spin statistics for pH_2 by only including the even rotational energy levels in the orientational average. Finally, the AHR-averaged NNP is generated, where pH_2 is a point-like and thus effective spherical particle (right panel).

to provide the reference data instead of electronic structure reference calculations to which the interim all-atom NNP has been fitted to provide $V(R,\theta,\phi,\theta',\phi')$. Therefore, the AHR-averaged NNP is directly obtained from the all-atom NNP through the AHR-averaged interaction energies.

III. COMPUTATIONAL DETAILS

The first step is to produce the all-atom NNP to describe the interaction between the solute molecule and H_2. This all-atom NNP is obtained starting from the potential energy surface that describes non-rigid solute species (which we represent here in terms of another highly accurate, intramolecular NNP published earlier[61]) in order to account for the flexibility of the molecule. The dataset is obtained using the automated procedure[42] developed for He atoms, which has been extended to work with the H_2 molecule, namely to consider its possible orientations around the solute molecule. The original procedure employed to select the position of the helium atoms is used to select the position of the center of mass of the H_2 molecule, and its orientation is then randomly generated centered on that point; note that this procedure can be readily generalized from diatomics to polyatomic solvents such as CH_4. It is important that all possible orientations of the H_2 molecule are properly represented in the all-atom NNP, since the subsequent AHR procedure averages over them and thus needs to rely on exhaustive angular information in order to accurately compute the matrix elements given by Eq. (3) using the all-atom NNP to represent $V(R,\theta,\phi,\theta',\phi')$. While building the dataset, all the configurations where H_2 is further away than 12 Å from the solute are excluded, as well as those for which the H_2 center of mass is closer than 2.05 Å to the O atom or 1.25 Å to the H atoms of the water and protonated water molecules, similarly to previous work for the NNP interaction potential of protonated water clusters in helium.[42]

The dataset for the $H_2O\cdots H_2$ all-atom NNP has been generated with 100 loops of the automated procedure adding 100 structures in each loop. The structures added in each loop have been sampled out of a set of 200 000 randomly generated configurations, which is reduced to a 100 by our active learning procedure. These pruning steps are urgently needed in order to reduce the computational effort of the demanding coupled cluster electronic structure calculation to a minimum of configurations while exhaustively sampling the relevant configuration space to fit the NNP. The generated dataset of structures is then randomly divided into a training set composed of 90 % of the selected structures and a test set containing the remaining 10 %. The fits of the NNP have been performed with the `RubNNet4MD` program[62] using an architecture of 3 hidden layers with 30 nodes each. A hyperbolic tangent activation function is used in all hidden layers and a linear one for the output layer. The weights of the NN are optimized by the element-decoupled Kalman filter.[63,64] A total of 10 different independent models have been generated that way and the committee approach[60] has been applied to obtain the final all-atom NNP as their average.

The same approach is used to generate the all-atom NNP for $H_3O^+\cdots H_2$, but only 60 loops of the automated procedure were performed resulting in a grand total of 59 800 selected structures. The all-atom and AHR-averaged final interaction NNPs for H_2O and H_3O^+ interacting with H_2 and pH_2, respectively, are provided as Supplementary Information to this paper.

The reference interaction energies have been computed using the coupled cluster method[65–67] with single, dou-

ble and scaled perturbative triple excitations, considered the 'gold standard' in quantum chemistry, using the F12a correction[68,69] subject to an adequate scaling of the triples[69] together with the aug-cc-pVTZ basis set.[70,71] The counterpoise (cp) correction[72] has been applied in order to correct for the remaining basis set superposition error, thus providing the CCSD(T*)-F12a/aVTZcp technique which we abbreviate simply by 'CC' for brevity, see also the Supplementary Information. All interaction energies have been computed with the `Molpro` program.[73,74]

In order to generate the AHR-averaged NNP for the interaction, it is firstly needed to evaluate the averaged interaction energy. This AHR average is performed using an in-house program coupled to the `CP2K` program,[75] which is used to evaluate the NNP energies of the all-atom system. In a first step, the Hamiltonian matrix

$$\langle \psi | \, \hat{T}_{pH_2} + \frac{\hbar^2}{2\mu R^2} \hat{j}^2_{pH_2} + V(R,\theta,\phi,\theta',\phi') \, | \psi \rangle \qquad (4)$$

is computed using a linear combination of spherical harmonics up to $l_{max} = 8$ to represent the eigenstates ψ as specified in Eq. (2). Importantly, only even values of l together with the corresponding m values are included in the sum as required to describe pH_2. The potential energy contribution according to Eq. (3) is integrated numerically using 32 Gauss-Legendre and 64 Gauss-Chebyshev quadrature points for the integration of θ' and ϕ' angles, respectively, where the all-atom $V(R,\theta,\phi,\theta',\phi')$ potential is represented using the all-atom NNP. Then, the Hamiltonian matrix is diagonalized in that basis and its lowest eigenvalue is the AHR-averaged energy, $V^{AHR}(R,\theta,\phi)$. More details on the convergence of the AHR average as a function of l_{max} and the number of quadrature points for the integration of the potential energy matrix elements can be found in the Supplementary Information.

The AHR-averaged NNP is obtained using the same automated procedure as in the all-atom version described above. The generation of the pH_2 center of mass positions is done analogously as in the original procedure for helium interactions[42] but using the same cutoffs as in the all-atom case as specified above. But now, our in-house AHR-averaging program is used in combination with the all-atom NNP to compute the reference energies instead of the highly accurate, but computationally expensive CCSD(T*)-F12a/aVTZcp calculations used for the generation of the all-atom NNP. Again, it is important to point out that the generation of the AHR-averaged interaction NNP is started from the solute's intramolecular NNP for both, H_2O and H_3O^+ as published earlier[61] in order to fully account for the flexibility of the molecules also when interacting with pH_2.

The AHR-averaged NNPs for $H_2O\cdots pH_2$ and $H_3O^+\cdots pH_2$ are obtained doing 60 loops of the automated procedure and adding 100 structures to the dataset in each loop. Similarly to the all-atom NNPs, the structures added in each loop have been sampled out of a set of 200 000 randomly-generated configurations, which is reduced to 100 by our active learning procedure. The fits to generate the AHR-averaged NNPs have been performed using NNPs composed of 2 hidden layers with 20 nodes each and the dataset has been divided again into a training set composed of 90 % of the structures and a test set containing the remaining 10 %.

Finally, the committee disagreement between the different all-atom NNP models has been used to remove highly distorted configurations from the AHR-averaged NNP dataset. Indeed a few unrealistically distorted configurations are selected by the automated procedure to fit the interaction NNP which, when included, only deteriorate the fit and decrease the overall accuracy of the resulting NNP rather than improving its quality. Such exotic $H_2O\cdots H_2$ or $H_3O^+\cdots H_2$ configurations arise when combining a high potential energy and thus low probability structure of the solute species – for instance a close to linear configuration of the H_2O molecule – with a rather low interaction energy of that quasi-linear H_2O with H_2. When fitting now the interaction NNP of H_2O with H_2, only the (favorably low) interaction energy is considered, while the (unrealistically high) potential energy of the bare solute molecule (which increases enormously the total potential energy of that $H_2O\cdots H_2$ complex) does not play any role. Describing these situations faithfully is demanding for the interaction NNP (if not exhaustively sampling them, which is not useful since the underlying solute configurations have negligible probability in any realistic simulation) and should be avoided at the outset. In order to systematically detect these unrealistic *solute*$\cdots$*solvent* configurations in an automated way, we use the committee disagreement between the 10 models that constitute the all-atom NNP. For each and every selected position of the H_2 center of mass, the interaction energy and the associated committee disagreement are evaluated for a total of $32 \cdot 64 = 2048$ different orientations of the H_2 molecule during the AHR averaging procedure. If any of those committee disagreements exceeds a certain cutoff value then the selected configuration is discarded. The committee disagreement cutoffs used for the AHR-averaged NNPs of $H_2O\cdots pH_2$ and $H_3O^+\cdots pH_2$ are 0.2 and 0.03 kcal/mol, respectively.

In order to explicitly validate the accuracy of the AHR-averaged NNPs for the present purpose, we computed the interaction potential for numerous positions of pH_2 on a cubic Cartesian grid around solute species H_2O and H_3O^+ frozen at their equilibrium structures using (i) the CC reference method (i.e. CCSD(T*)-F12a/aVTZcp throughout including explicit AHR averaging), (ii) the all-atom NNP + AHR and (iii) the AHR-averaged NNP. Additionally, (iv) the AHR-averaged potential from Ref. 48 has also been used for $H_2O\cdots pH_2$ since it has been obtained using a similar electronic structure methodology, while freezing the H_2O configuration in its equilibrium structure. This cubic grid approach allows for the simulation of pH_2 microsolvation around a frozen molecule in order to validate the quality of the NNP representation of the interaction potential, which cannot be done using CC reference calculations on-the-fly as the path integral simulations proceed. The cubic grid is generated with 43 grid points in each dimension, a grid spacing of 0.28 Å, and a cutoff of 2.5 Å around the center of mass of the frozen solute molecule within which the interaction potential is not evaluated. This cutoff does not induce any error in our calculations because the energies are

highly repulsive at short distances and, thus, the simulations do not sample this part of the potential energy surface. The use of this cutoff reduces the computational effort, but this is still not enough to sufficiently reduce the computational load to carry out the required number of coupled cluster calculations on that grid. Of course we also take advantage of symmetry elements of these two molecules at their equilibrium structures, which all together allows for the saving of more than 75 % of the grid point calculations for water, reducing the number of calculations from almost 84 000 down to about 20 000, and 50 % for protonated water, so about 40 000 calculations are necessary. On top of that, the number of Gauss-Legendre and Gauss-Chebyshev grid points for the integration of the potential energy term in the AHR averaging is reduced from 64 and 32 to 20 and 10, respectively, but only for the generation of the validation data on that grid; we are confident that this reduction in quadrature accuracy will not have any significant impact on our validation of the microsolvation of H_2O and H_3O^+ with pH_2 since we show in the Supplementary Information that the AHR-averaged interaction energies are basically converged for these reduced values. All together, these savings make the generation of the CCSD(T*)-F12a/aVTZcp AHR-averaged data on a grid computationally affordable, although it required roughly 4 and 8 million single-point CC energy calculations for the frozen H_2O and H_3O^+ configurations, respectively.

All Path Integral (PI) simulations have been performed with the `CP2K` simulation package,[75] where a NNP extension for the interaction potential has been implemented by some of us. The PI calculations on a grid for the purpose of explicit application of the two AHR-averaged NNPs have been performed using water and protonated water molecules frozen in their minimum energy structure surrounded by 1 to 30 point-like pH_2 molecules. A bosonic PIMC sampling scheme is used for pH_2, whose $pH_2\cdots pH_2$ interactions in the PI action are treated using the pair density matrix approximation[76,77] and described by the Silvera-Goldman pairwise interaction potential.[50] The *solute*$\cdots pH_2$ interactions are evaluated on the grid using nearest-neighbor interpolation. The temperature is set to 1 K and 80 beads are used to discretize the pair density matrix. A total number of 40 independent PIMC walkers are generated for the sampling of pH_2 together with the worm algorithm[78,79] allowing for bosonic exchange. We refer the interested reader to Ref. 41 where our underlying simulation technique is reviewed including our extension of worm sampling.

IV. RESULTS AND DISCUSSION

To illustrate the capabilities of our methodology, we have applied it to the $H_2O\cdots pH_2$ and $H_3O^+\cdots pH_2$ interactions. We chose $H_2O\cdots pH_2$ since it is the same system as studied in the original work introducing the AHR averaging procedure.[48] This makes the water molecule particularly useful for us as a benchmark to assess the accuracy of our approach. While the original AHR procedure relied on the rigid rotor approximation for the impurity — being very reasonable for quasi-rigid species such as the H_2O molecule — our approach includes the full flexibility of the solute of choice. For these reasons, we have also developed an AHR-averaged NNP for $H_3O^+\cdots pH_2$, as the hydronium cation is governed by large-amplitude umbrella inversion motion. Furthermore, the application to the more weakly and strongly interacting dopants H_2O and H_3O^+, respectively, while fully accounting for stiff intramolecular flexibility as well as floppiness highlights the general nature of our data-driven procedure.

A. $H_2O\cdots pH_2$ interaction and microsolvation

We start by applying the methodology described above to the $H_2O\cdots pH_2$ interaction potential. The main reason for selecting this system is to benchmark our method against the already available AHR-averaged interaction potential,[48] which is based on a 5-dimensional interaction potential of a rigid water molecule fitted to accurate coupled cluster reference calculations.[80] The electronic structure setup used for these reference calculations is very comparable to the more recent CCSD(T*)-F12a/aVTZcp technique underlying our development of the all-atom interaction NNP. This makes the water system the perfect candidate to serve as benchmark of our AHR-averaged interaction NNP.

The all-atom NNP underlying the generation of our final $H_2O\cdots pH_2$ interaction potential has been trained on a dataset containing 150 768 structures that have been selected during our automated and data-driven machine learning protocol. This interaction potential has a training error of 1.4×10^{-2} kcal/mol and a similar test error of 1.4×10^{-2} kcal/mol, which is well below what is considered to correspond to chemical accuracy (1 kcal/mol). The accuracy of our all-atom interaction potential is highlighted in the left panel of Figure 2 by different measures based on the comparison of CC reference interaction energies with the all-atom NNP prediction. The nearly perfect correlation of the interaction energies showcases the robust description of both, the attractive and repulsive regions of the interaction potential. The errors over the full range of interactions (left, bottom) reveals no outlier, while the error distribution features a sharp peak very close to zero with tails that barely cross 0.01 kcal/mol. We refer the interested reader to the Supplementary Information for additional tests of the all-atom NNP, including angular and radial scans that explicitly probe distinctly different regions of this interaction potential.

Using the carefully benchmarked all-atom NNP, we proceeded to generate the AHR-averaged NNP to describe the $H_2O\cdots pH_2$ interaction. The AHR-averaged NNP relies on a dataset containing 59 933 structures, again selected using our automated machine learning procedure. The fit is subject to a training and a test error of 3.5×10^{-3} and 3.9×10^{-3} kcal/mol, respectively. The accuracy of the AHR-averaged interaction energies is illustrated in Figure 2 (right). We find close to perfect correlation between the AHR-energies computed with the all-atom NNP, which provides the reference data in this case, and the AHR-averaged NNP prediction and very narrow error distributions, while no outliers are observed over

the full range of interactions. We mention in passing that the committee-based approach to identify unrealistically distorted solute configurations within the *solute*$\cdots$H$_2$ complexes as described in Section III turned out to be mandatory in order to achieve such high quality fits.

Let us next concentrate on an in-depth benchmark of the interaction potentials. Usually, this would entail to perform the desired simulations to probe various properties of the system of interest with the developed models as well as explicitly using the reference method on-the-fly as customarily done when using computationally economical DFT-based electronic structure to provide the reference data. However, this would require the computation of the AHR-average using the reference CCSD(T*)-F12a/aVTZcp method directly. Unfortunately, this is out of scope, as roughly 2000 such CC calculations are needed for each center of mass position of the pH$_2$ species to sample the underlying H$_2$ orientations for each and every *solute*$\cdots p$H$_2$ configuration generated during the path integral simulation, which easily extends to millions of such single-point calculations for a typical HPIMD/MC simulation. A more realistic option is to compare radial and angular scans or two-dimensional cuts of the full-dimensional interaction potential energy surface using the all-atom NNP to evaluate the AHR-average along these scans and cuts as we indeed show in the Supplementary Information. However, this only allows for the testing of a small part of the relevant configuration space and, moreover, does not consider the indirect impact of the pH$_2\cdots p$H$_2$ interactions which greatly interplay with the *solute*$\cdots p$H$_2$ interactions . Recall that the spatial structure of quantum clusters at low temperature can be distinctly different from their structure in global and even low-energy local minima of their potential energy surface due to the severe quantum delocalization of light particles such as pH$_2$ or also He.

Taking these considerations into account, we resort to another approach as originally introduced in Ref. 81 and successfully applied in the context of helium (micro)solvation.[42] By evaluating the interaction potential for a fixed configuration of the solute on a relatively coarse grid using the CC reference method, the *solute*$\cdots p$H$_2$ interaction potential can efficiently be mapped, enabling the evaluation of the interaction energy on that grid during exhaustive PIMC sampling of the pH$_2$ solvent (while using nearest-neighbor interpolation between the grid points). This method allows us to study microsolvation of the solute in a frozen configuration using different numbers of pH$_2$ molecules. From those calculations we can compute the spatial distribution function (SDF), a property that is known to be highly sensitive to small changes in the interaction potential in particular for quantum clusters for said reasons. Furthermore, it is possible to use this approach for both, the all-atom and the AHR-averaged NNP, providing a consistent benchmark over the entire process of the generation of the AHR-averaged NNP starting from the CC reference calcuations. We stress that these unusually stringent benchmarks still remain unpleasantly expensive since they require roughly 4 to 8 million CC energy calculations for the selected frozen solute configurations. Note that this drastically exceeds the number of CC calculations performed for the development of the NNPs in the first place, which grants access to fully flexible solute species in HPIMD/MC simulations.

The SDFs for H$_2$O(pH$_2$)$_N$ have been computed from path integral simulations using $N = 1$ up to 30 pH$_2$ molecules with the interaction energy computed in four different ways as depicted from top to bottom in Figure 3: (i) using the reference CC method and performing the AHR-average explicitly based on single-point CC calculations to sample the orientations at each center of mass position, (ii) performing the AHR-average but using the all-atom NNP interaction energies, (iii) using directly the AHR-averaged NNP, and (iv) with the published AHR-averaged potential from Ref. 48. The comparison of the obtained SDFs allows for the analysis of the quality of the all-atom and the AHR-averaged NNP fits with respect to the highly accurate CC reference calculations as well as to the AHR-averaged potential available in the literature.[48] The results for selected clusters with $N = 5$, 12 and 30 pH$_2$ are shown in Figure 3 from left to right, while other SDFs are presented in the Supplementary Information. Overall, this stringent test highlights the high quality of the generated interaction potentials as there are no significant deviations between the SDFs obtained with the four methods. Only for the larger cluster size some slight differences can be observed with minor variations in the population of the second solvation shell. This has already been seen and discussed in a previous study for the case of helium solvation of protonated water clusters[42] and traced back to the high sensitivity of the SDFs to the chosen isovalues for large N where the density modulations in three-dimensional space fade out in conjunction with using a rather coarse Cartesian grid with a spacing of 0.28 Å. For $N = 30$, the slightly larger population of the interconnections between most populated regions in the second solvation shell reveals that the all-atom and the AHR-averaged NNPs have slightly higher interaction energies than the CC reference in those regions, whereas the AHR-averaged potential from Ref. 48 shows a shallower energy surface compared to our CC benchmark. Despite these small variations, the overwhelming agreement between the different approaches validates the accurate nature of our approach thus providing overall CCSD(T*)-F12a/aVTZcp quality for such quantum simulations.

B. $H_3O^+\cdots pH_2$ interaction and microsolvation

We move on to apply the developed methodology to the more challenging case of the H$_3$O$^+\cdots p$H$_2$ interaction potential. The positive charge of this solute gives rise to significantly stronger and more anisotropic interactions with the solvent. Furthermore, the solute is governed by its large-amplitude umbrella inversion whereby the three protons move across the coplanar transition state on the potential energy surface. Therefore, in this case and for any other species subject to large-amplitude motion, it is of crucial importance to include the flexibility of the molecule in the interaction potential – as done in our data-driven approach – to study its solvation by pH$_2$ or other weakly interacting solvents.

As before, the first step in our approach is the development

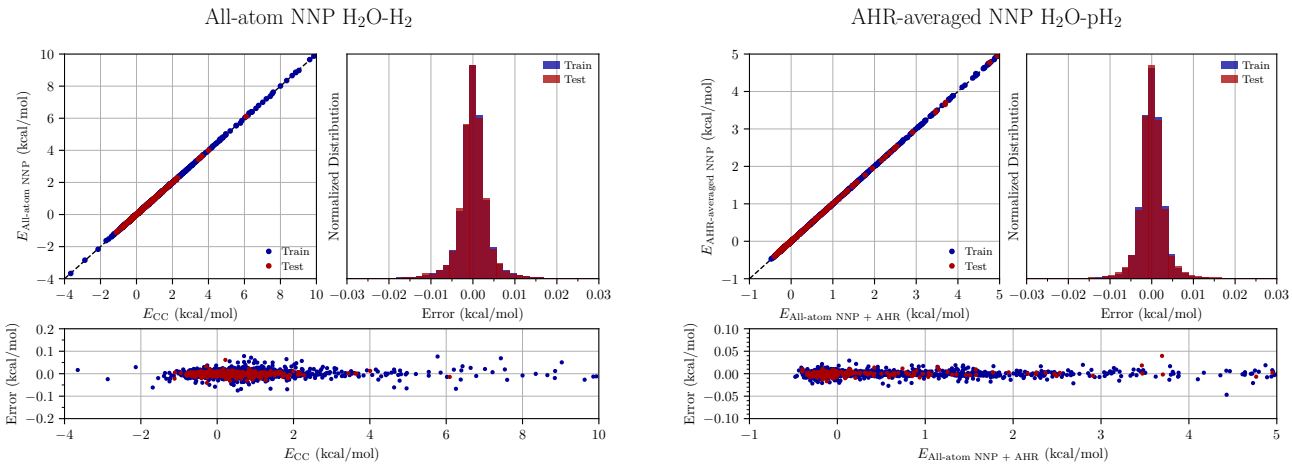

FIG. 2. Accuracy of the all-atom $H_2O\cdots H_2$ (left) and AHR-averaged $H_2O\cdots pH_2$ (right) NNPs, see text for discussion. Reference energies have been computed using CCSD(T*)-F12a/aVTZcp for the all-atom NNP, while the AHR-averaged energies based on the all-atom NNP are used as reference for the AHR-averaged NNP.

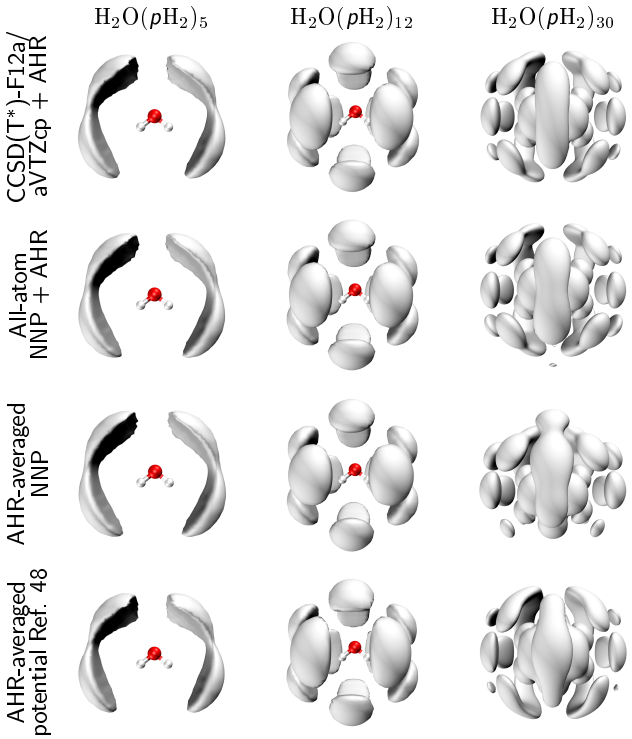

FIG. 3. Comparison of the pH_2 SDFs around frozen H_2O on a grid, see text, obtained with different methods to compute the interactions for three cluster sizes N. From top to bottom: (i) CCSD(T*)-F12a/aVTZcp + AHR-averaging, (ii) all-atom $H_2O\cdots pH_2$ NNP + AHR averaging, (iii) AHR-averaged $H_2O\cdots pH_2$ NNP, and (iv) AHR-averaged potential from Ref. 48. From left to right: $N = 5$, 12 and 30 pH_2 molecules solvating the minimum energy structure of the water molecule. The isovalues are 0.0065, 0.0090, and 0.0030 1/bohr^3 for $N = 5$, 12 and 30.

of the all-atom NNP. This model has been trained on a dataset of 59 800 structures, again selected in our automated procedure . It might appear surprising at first sight that much less reference data were needed for H_3O^+ compared to H_2O but the reason is that the much more shallow interaction potential energy surface in the latter case needs to be sampled much more densely to train the all-atom NNP to the desired accuracy. The resulting model has a training and a test error of 6.5×10^{-2} and 6.2×10^{-2} kcal/mol respectively. The quality of the training of the full dimensional interaction potential is illustrated in Figure 4 (left), which shows a near perfect correlation and together with a very narrow error distribution.

In the next step, the AHR-averaged NNP has been trained using a dataset containing 57 616 structures, selected as before with our automated procedure. The resulting training and test errors are 6.0×10^{-3} and 6.4×10^{-3} kcal/mol, respectively. The accuracy of this fit is of the same order of magnitude as that of the AHR-averaged $H_2O\cdots pH_2$ fit and it is again well below chemical accuracy. This very good accuracy is demonstrated in Figure 4 (right), where almost perfect correlation between the AHR-averaged energies computed a posteriori from the all-atom NNP and the predicted energies from the AHR-averaged NNP is seen. Furthermore, no outlier can be observed and the error distribution is very narrow with its tail being negligible for errors larger than 0.025 kcal/mol. Again, it was decisive to remove the strongly distorted solute configurations when fitting its interaction potential with pH_2.

We again resort to the comparison of pH_2 SDFs for an in-depth benchmark of the performance of our models in path integral simulations using $N = 1$ up to 30 pH_2 molecules around frozen H_3O^+. These SDFs are used to validate the accuracy of the NNP at the three different stages of our approach: (i) using the reference CCSD(T*)-F12a/aVTZcp method and performing the AHR-average with the obtained energies, (ii) performing the AHR-average using the all-atom NNP, and (iii)

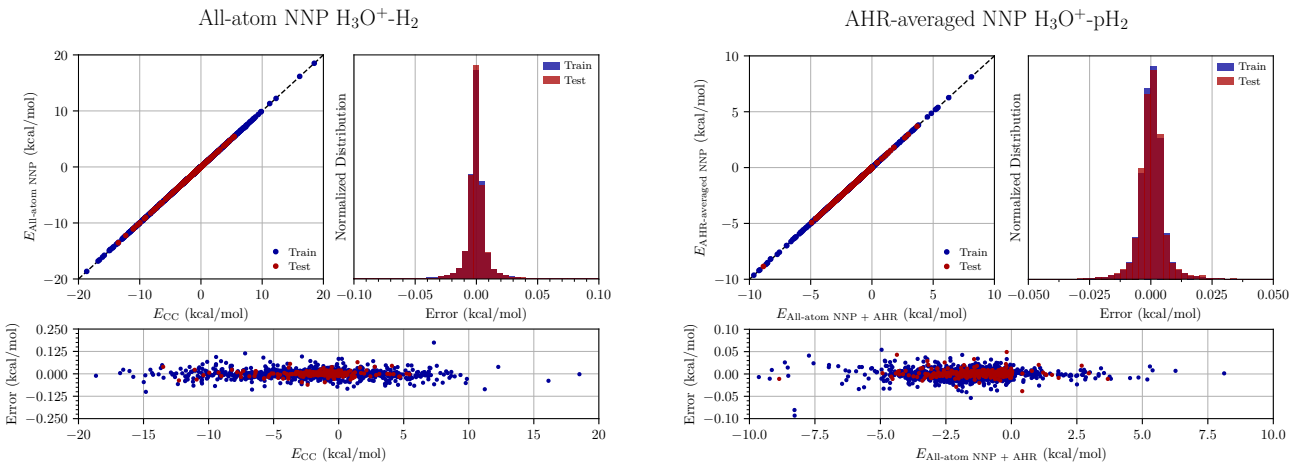

FIG. 4. Accuracy of the all-atom $H_3O^+\cdots H_2$ (left) and AHR-averaged $H_3O^+\cdots pH_2$ (right) NNPs, see text for discussion. Reference energies have been computed using CCSD(T*)-F12a/aVTZcp for the all-atom NNP, while the AHR-averaged energies based on the all-atom NNP are used as reference for the AHR-averaged NNP.

with the AHR-averaged NNP. As this approach requires to use the solute with a fixed structure, we are considering the protonated water molecule in its minimum energy configuration for that purpose. The results for the clusters with $N = 5$, 12 and 30 pH_2 are shown in Figure 5 whereas more are compiled in the Supplementary Information. Overall, there are no significant deviations between the three methods, except for some small differences similar to what has been observed for water, again factoring in the resolution due to a grid spacing of 0.28 Å. This highlights also for this case the high quality of the generated AHR-averaged NNP.

Finally, we illustrate the importance of including the flexibility of the protonated water molecule in our data-driven generation of the interaction potentials by computing the pH_2 SDFs with the AHR-averaged NNP along the reaction coordinate of the large-amplitude umbrella motion. We restrict this analysis to $N = 5$ and 12 pH_2 molecules, but compute the SDFs for different configurations of H_3O^+ along the umbrella inversion coordinate. These SDFs are shown in Figure 6 for a set of configurations along the umbrella inversion path of the bare protonated water molecule together with the associated potential energy profile of bare H_3O^+ (obtained from its NNP published earlier[61]). Here, this coordinate is defined as the dihedral angle of the four atoms, which provides the deviation from planarity of the molecule; note that the OH bond distances are kept at the value of the minimum energy configuration. It can be easily seen that the structure of the H_3O^+ molecule has a major impact on the spatial distribution of the solvating pH_2 molecule, thus highlighting the importance of including the flexibility of the solvent in the generation of the AHR-averaged NNP. For the fully planar H_3O^+ transition state-like structure of $H_3O^+(pH_2)_5$, see point (4) in the top panels of Figure 6, we observe a torus-like distribution of pH_2 within the plane of the flat solute molecule. Next, upon moving away from the transition state toward either side along

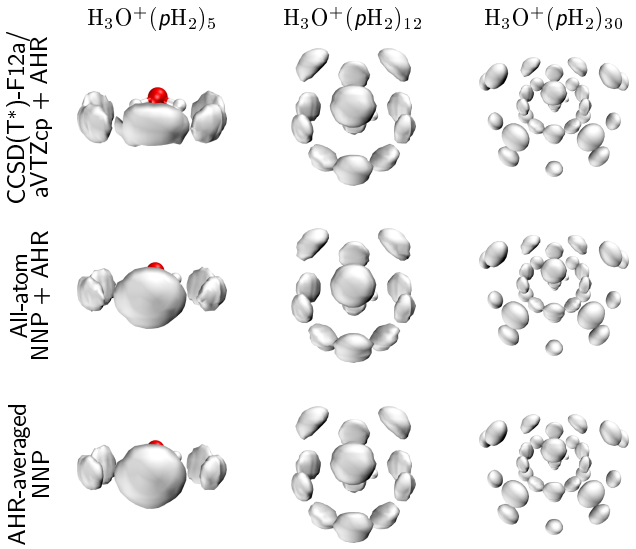

FIG. 5. Comparison of the pH_2 SDFs around frozen H_3O^+ on a grid, see text, obtained with different methods to compute the interactions for three cluster sizes N. From top to bottom: (i) CCSD(T*)-F12a/aVTZcp + AHR-averaging, (ii) all-atom $H_3O^+\cdots pH_2$ NNP + AHR averaging, and (iii) AHR-averaged $H_3O^+\cdots pH_2$ NNP. From left to right: $N = 5$, 12 and 30 pH_2 molecules solvating the minimum energy structure of the protonated water molecule. The isovalues are 0.0250 1/bohr^3 for the three complexes.

the energy path, the pH_2 density initially follows the displacement of the protons while preserving the torus-like topology, which also characterizes the equilibrium structure of the $N = 5$ cluster at the global minimum structure reached at points (2) and (6). However, as the protons of H_3O^+ come closer to each other as a result of increasing the pyramidal character of

H_3O^+ further, the pH_2 torus gets strongly compressed resulting in the displacement of one pH_2 molecule out of the ring as seen for the first and last SDFs with five pH_2 at points (1) and (7).

A similar but even more complex scenario is observed with $N = 12$ pH_2 molecules around H_3O^+, see bottom panels. While the planar transition state at point (1) again shows a fully symmetric SDF including also the second solvation shell, when deviating from it, the SDF symmetry gets broken: Most of the pH_2 density gets more and more accumulated on the side of H_3O^+ where the protons are, thus leaving the oxygen side less solvated at points (1) and (7). We note that the potential energy difference between these selected points (1) and (7) w.r.t. the equilibrium structure (2) and (6) is smaller than that of the transition state (4) that governs the umbrella dynamics of bare H_3O^+. In other words: The qualitative changes of the first and second microsolvation shell of these quantum clusters that we disclose here are not high-energy and thus unrealistic phenomena at temperatures on the order of 1 K, but are expected to be highly relevant when immersing a fluxional dopant such as H_3O^+ in ultracold pH_2 environments. More generally speaking, this comparison highlights the potential of our overall approach to elucidate the coupling between bosonic pH_2 environments and the (ro-)vibrational motion of non-rigid molecular impurities being subject to large-amplitude motion and floppiness, while it consistently also covers the limit of quasi-rigid molecules as demonstrated here for H_2O.

V. SUMMARY AND CONCLUSIONS

In this work we have shown how highly accurate *impurity*$\cdots pH_2$ interaction potentials, which include the full flexibility of non-rigid molecular impurities and implement the nuclear spin statistics of this solvent species, can be developed in a data-driven manner based on largely automated machine learning techniques. These high-dimensional neural network potentials (NNPs) enable converged quantum simulations of the corresponding para-hydrogen clusters, *impurity*$(pH_2)_N$, from the tagging limit for small N via the intermediate microsolvation regime to finally bulk-like nanodroplet solvation for very large solvent numbers. We achieve this task in a three step process, where we start by generating an all-atom NNP for the interaction between the molecular solute impurity and an H_2 molecule fitted to accurate coupled cluster electronic structure calculations, here CCSD(T*)-F12a/aVTZcp. Next, using this all-atom NNP, we obtain an effective point-particle description of pH_2 by averaging over all orientiations of the two-site H_2 molecule. Including only the even rotational quantum states in that anisotropic quantum average properly accounts for the nuclear spin statistics of pH_2 within the adiabatic hindered rotor (AHR) approximation. Finally, we train the *impurity*$\cdots pH_2$ AHR-averaged interaction potential to these efficiently generated AHR-averaged energies, resulting in the corresponding single-site AHR-averaged NNP. Most parts of this process are fully automated, thus enabling à la carte generation of AHR-averaged NNPs from quasi-rigid to highly fluxional molecular species or complexes.

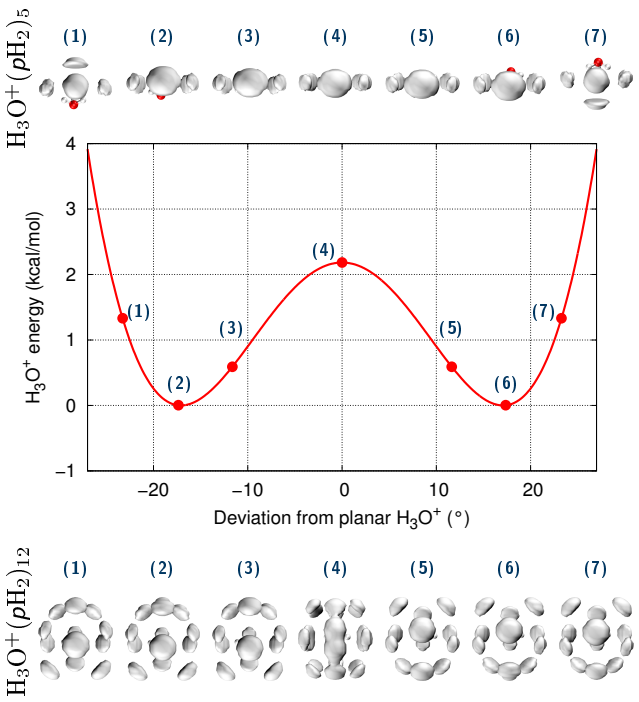

FIG. 6. Comparison of the pH_2 SDFs around H_3O^+ on a grid obtained with the AHR-averaged NNP for different protonated water structures along the umbrella inversion coordinate of bare H_3O^+, defined as the dihedral angle of the four atoms, which provides the deviation from planarity of the molecule; note that the OH bond distances are kept at the value of the minimum energy configuration, see text, for $N = 5$ (top) and 12 (bottom) pH_2 molecules together with the corresponding intramolecular potential energy profile of bare H_3O^+ in the middle panel. The SDF isovalues are 0.0250 1/bohr^3 for the two cluster sizes.

With the aim of showing the capabilities of our data-driven methodology, we have applied it to the $H_2O\cdots pH_2$ and $H_3O^+\cdots pH_2$ interactions to represent the class of quasi-rigid and non-rigid molecular dopants, respectively, for which we analyze the accuracy of each step of the process. Detailed comparison of the prediction of the developed NNP models highlights the capability of our approach to retain coupled cluster accuracy up to the level of the AHR-averaged NNPs. Going beyond energetic error assessments, we also show that the pH_2 probability densities within the $H_2O(pH_2)_N$ and $H_3O^+(pH_2)_N$ complexes with frozen solute impurities, as sampled from path integral simulations at 1 K including the bosonic exchange of pH_2, are in very good agreement with the corresponding spatial distribution functions (SDFs) for different cluster sizes N obtained when explicitly using the coupled cluster reference method including explicit AHR-averaging. This makes us confident that our approach holds great promise for the development of highly accurate pH_2 interaction potentials for a wide variety of systems.

Going beyond the rigid-rotor approximation, usually employed in the field, our method accounts for the full flexibility

of the solute of interest from small- up to large-amplitude motion. Although certainly not crucial for quasi-rigid impurities such as water, considering the (ro-)vibrational dynamics of the solute species is of great importance for fluxional systems, which are completely dominated by large-amplitude motion, such as the studied hydronium cation. Therefore, our methodology enables accurate investigations of (micro-)solvation phenomena of complex molecular species and complexes in $p\mathrm{H}_2$ environments from the tagging limit up to nanoscale solvation at ultra-low temperatures, while fully accounting for the flexibility of the impurity and the bosonic nature of $p\mathrm{H}_2$.

SUPPLEMENTARY MATERIAL

The all-atom (AA) and AHR-averaged final interaction NNPs for $\mathrm{H_2O}$ and $\mathrm{H_3O^+}$ interacting with H_2 and $p\mathrm{H}_2$, respectively, are prodivded as separate supplementary material data files as follows:
NN-IP-H2O-H2-AA-2022-V1,
NN-IP-H2O-PH2-AHR-2022-V1,
NN-IP-H3OP-H2-AA-2022-V1,
NN-IP-H3OP-PH2-AHR-2022-V1
whereas additional information and analyses are provided in a separate PDF document.

ACKNOWLEDGMENTS

We would like to thank Harald Forbert for many insightful discussions on this topic as well as for most valuable technical help. We are particularly grateful to Pierre-Nicholas Roy for providing us with the AHR-averaged interaction potential for $\mathrm{H_2O}\cdots p\mathrm{H}_2$ as published in Ref. 48 and for granting us permission to use and publish the data we obtained using this potential in Figure 3. Partially funded by the *Deutsche Forschungsgemeinschaft* (DFG, German Research Foundation) via the DFG grant MA 1547/19 to D.M., by the DFG under Germany's Excellence Strategy – EXC 2033 – 390677874 – RESOLV, and supported by the "Center for Solvation Science ZEMOS" funded by the German Federal Ministry of Education and Research and by the Ministry of Culture and Research of North Rhine-Westphalia. C.S. acknowledges partial financial support from the *Alexander von Humboldt-Stiftung*. The computational resources were provided by HPC@ZEMOS, HPC-RESOLV, and BoViLab@RUB.

AUTHOR DECLARATIONS

Conflict of Interest

The authors have no conflicts to disclose

DATA AVAILABILITY STATEMENT

Data available in article or supplementary material

[1] P. Kapitza, Nature **141**, 74 (1938).
[2] J. F. Allen and A. Misener, Nature **141**, 75 (1938).
[3] V. L. Ginzburg and A. A. Sobyanin, Sov. Phys. JETP Lett. **15**, 242 (1972).
[4] S. Grebenev, B. Sartakov, J. P. Toennies, and A. F. Vilesov, Science **289**, 1532 (2000).
[5] P. Sindzingre, D. M. Ceperley, and M. L. Klein, Phys. Rev. Lett. **67**, 1871 (1991).
[6] H. Li, X.-L. Zhang, T. Zeng, R. J. Le Roy, and P.-N. Roy, Phys. Rev. Lett. **123**, 093001 (2019).
[7] I. F. Silvera, Rev. Mod. Phys. **52**, 393 (1980).
[8] D. Scharf, M. L. Klein, and G. J. Martyna, J. Chem. Phys. **97**, 3590 (1992).
[9] F. Mezzacapo and M. Boninsegni, Phys. Rev. Lett. **97**, 045301 (2006).
[10] F. Mezzacapo and M. Boninsegni, Phys. Rev. A **75**, 033201 (2007).
[11] S. A. Khairallah, M. B. Sevryuk, D. M. Ceperley, and J. P. Toennies, Phys. Rev. Lett. **98**, 183401 (2007).
[12] F. Mezzacapo and M. Boninsegni, Phys. Rev. Lett. **100**, 145301 (2008).
[13] J. E. Cuervo and P.-N. Roy, J. Chem. Phys. **125**, 124314 (2006).
[14] H. Li, R. J. Le Roy, P.-N. Roy, and A. R. W. McKellar, Phys. Rev. Lett. **105**, 133401 (2010).
[15] T. Zeng and P.-N. Roy, Rep. Prog. Phys. **77**, 046601 (2014).
[16] M. Schmidt, J. M. Fernández, N. Faruk, M. Nooijen, R. J. Le Roy, J. H. Morilla, G. Tejeda, S. Montero, and P.-N. Roy, J. Phys. Chem. A **119**, 12551 (2015).
[17] M. Schmidt and P.-N. Roy, J. Chem. Phys. **156**, 016101 (2022).
[18] V. E. Bondybey, A. M. Smith, and J. Agreiter, Chem. Rev. **96**, 2113 (1996).
[19] T. Momose, M. Fushitani, and H. Hoshina, Int. Rev. Phys. Chem. **24**, 533 (2005).
[20] M. Okumura, L. I. Yeh, J. D. Myers, and Y. T. Lee, J. Chem. Phys. **85**, 2328 (1986).
[21] S. Chakrabarty, M. Holz, E. K. Campbell, A. Banerjee, D. Gerlich, and J. P. Maier, J. Phys. Chem. Lett. **4**, 4051 (2013).
[22] A. B. Wolk, C. M. Leavitt, E. Garand, and M. A. Johnson, Acc. Chem. Res. **47**, 202 (2014).
[23] D. Scharf, G. J. Martyna, and M. L. Klein, Chem. Phys. Lett. **197**, 231 (1992).
[24] J. E. Cuervo and P.-N. Roy, J. Chem. Phys. **128**, 224509 (2008).
[25] M. C. Gordillo, Phys. Rev. B **60**, 6790 (1999).
[26] C. Cazorla and J. Boronat, Phys. Rev. B **78**, 134509 (2008).
[27] J. E. Cuervo and P.-N. Roy, J. Chem. Phys. **131**, 114302 (2009).
[28] Y. Kwon and K. B. Whaley, Phys. Rev. Lett. **89**, 273401 (2002).
[29] M. P. de Lara-Castells and A. O. Mitrushchenkov, J. Phys. Chem. Lett. **2**, 2145 (2011).
[30] H. Li, A. R. W. McKellar, R. J. Le Roy, and P.-N. Roy, J. Phys. Chem. A **115**, 7327 (2011).
[31] P. L. Raston, W. Jäger, H. Li, R. J. Le Roy, and P.-N. Roy, Phys. Rev. Lett. **108**, 253402 (2012).
[32] C. H. Mak, S. Zakharov, and D. B. Spry, J. Chem. Phys. **122**, 104301 (2005).
[33] T. Zeng, G. Guillon, J. T. Cantin, and P.-N. Roy, J. Phys. Chem. Lett. **4**, 2391 (2013).
[34] T. Zeng, H. Li, and P.-N. Roy, J. Phys. Chem. Lett. **4**, 18 (2012).
[35] T. Zeng, N. Blinov, G. Guillon, H. Li, K. P. Bishop, and P.-N. Roy, Comput. Phys. Commun. **204**, 170 (2016).
[36] L. Walewski, H. Forbert, and D. Marx, Comput. Phys. Commun. **185**, 884 (2014).
[37] L. Walewski, H. Forbert, and D. Marx, J. Chem. Phys. **140**, 144305 (2014).
[38] A. Witt, S. D. Ivanov, and D. Marx, Phys. Rev. Lett. **110**, 083003 (2013).
[39] F. Uhl and D. Marx, Angew. Chem. Int. Ed. **57**, 14792 (2018).
[40] F. Uhl and D. Marx, Phys. Rev. Lett. **123**, 123002 (2019).
[41] F. Brieuc, C. Schran, F. Uhl, H. Forbert, and D. Marx, J. Chem. Phys. **152**, 210901 (2020).
[42] C. Schran, F. Uhl, J. Behler, and D. Marx, J. Chem. Phys. **148**, 102310 (2018).
[43] F. Paesani, R. E. Zillich, and K. B. Whaley, J. Chem. Phys. **119**, 11682 (2003).

[44]F. Paesani, R. E. Zillich, Y. Kwon, and K. B. Whaley, J. Chem. Phys. **122**, 181106 (2005).
[45]Y. Kwon and K. B. Whaley, J. Low Temp. Phys. **140**, 227 (2005).
[46]S. Moroni, M. Botti, S. De Palo, and A. R. W. McKellar, J. Chem. Phys. **122**, 094314 (2005).
[47]C. Piccarreta and F. A. Gianturco, Eur. Phys. J. D **37**, 93 (2006).
[48]T. Zeng, H. Li, R. J. Le Roy, and P.-N. Roy, J. Chem. Phys. **135**, 094304 (2011).
[49]H. Li, P.-N. Roy, and R. J. Le Roy, J. Chem. Phys. **133**, 104305 (2010).
[50]I. F. Silvera and V. V. Goldman, J. Chem. Phys. **69**, 4209 (1978).
[51]K. Patkowski, W. Cencek, P. Jankowski, K. Szalewicz, J. B. Mehl, G. Garberoglio, and A. H. Harvey, J. Chem. Phys. **129**, 094304 (2008).
[52]A. Ibrahim and P.-N. Roy, J. Chem. Phys. **156**, 044301 (2022).
[53]L. Wang, D. Xie, R. J. Le Roy, and P.-N. Roy, J. Chem. Phys. **139**, 034312 (2013).
[54]X.-L. Zhang, Y.-T. Ma, Y. Zhai, and H. Li, J. Chem. Phys. **148**, 124302 (2018).
[55]J. Behler and M. Parrinello, Phys. Rev. Lett. **98**, 146401 (2007).
[56]J. Behler, Angew. Chem. Int. Ed. **56**, 12828 (2017).
[57]J. Behler, Chem. Rev. **121**, 10037 (2021).
[58]P. Diep and J. K. Johnson, J. Chem. Phys. **112**, 4465 (2000).
[59]J. Behler, J. Chem. Phys. **134**, 074106 (2011).
[60]C. Schran, K. Brezina, and O. Marsalek, J. Chem. Phys. **153**, 104105 (2020).
[61]C. Schran, J. Behler, and D. Marx, J. Chem. Theory Comput. **16**, 88 (2020).
[62]F. Brieuc, C. Schran, H. Forbert, and D. Marx, "RubNNet4MD: Ruhr-Universität Bochum Neural Networks for Molecular Dynamics Software Package Version 1. 2020," https://www.theochem.rub.de/go/rubnnet4md.html.
[63]T. B. Blank and S. D. Brown, J. Chemom. **8**, 391 (1994).
[64]M. Gastegger and P. Marquetand, J. Chem. Theory Comput. **11**, 2187 (2015).
[65]J. Čížek, J. Chem. Phys. **45**, 4256 (1966).
[66]R. J. Bartlett, J. Phys. Chem. **93**, 1697 (1989).
[67]R. J. Bartlett and M. Musial, Rev. Mod. Phys. **79**, 291 (2007).
[68]T. B. Adler, G. Knizia, and H. J. Werner, J. Chem. Phys. **127**, 221106 (2007).
[69]G. Knizia, T. B. Adler, and H.-J. Werner, J. Chem. Phys. **130**, 054104 (2009).
[70]R. A. Kendall, T. H. Dunning, and R. J. Harrison, J. Chem. Phys. **96**, 6796 (1992).
[71]D. E. Woon and T. H. Dunning, J. Chem. Phys. **100**, 2975 (1994).
[72]S. F. Boys and F. Bernardi, Mol. Phys. **19**, 553 (1970).
[73]H. J. Werner, P. J. Knowles, G. Knizia, F. R. Manby, and M. Schütz, Wiley Interdiscip. Rev. Comput. Mol. Sci. **2**, 242 (2012).
[74]H.-J. Werner, P. J. Knowles, F. R. Manby, J. A. Black, K. Doll, A. Heßelmann, D. Kats, A. Köhn, T. Korona, D. A. Kreplin, Q. Ma, T. F. Miller, A. Mitrushchenkov, K. A. Peterson, I. Polyak, G. Rauhut, and M. Sibaev, J. Chem. Phys. **152**, 144107 (2020).
[75]CP2K Developers Team, http://www.cp2k.org.
[76]E. L. Pollock and D. M. Ceperley, Phys. Rev. B **30**, 2555 (1984).
[77]D. M. Ceperley, Rev. Mod. Phys. **67**, 279 (1995).
[78]M. Boninsegni, N. Prokof'ev, and B. Svistunov, Phys. Rev. Lett. **96**, 070601 (2006).
[79]M. Boninsegni, N. V. Prokof'ev, and B. V. Svistunov, Phys. Rev. E **74**, 036701 (2006).
[80]P. Valiron, M. Wernli, A. Faure, L. Wiesenfeld, C. Rist, S. Kedžuch, and J. Noga, J. Chem. Phys. **129**, 134306 (2008).
[81]D. Kuchenbecker, F. Uhl, H. Forbert, G. Jansen, and D. Marx, Phys. Chem. Chem. Phys. **19**, 8307 (2017).

SUPPORTING INFORMATION

Neural Network Interaction Potentials for *para*-Hydrogen with Flexible Molecules

Laura Durán Caballero,[1] Christoph Schran,[1,a)] Fabien Brieuc[1,b)] and Dominik Marx*[1]

[1] *Lehrstuhl für Theoretische Chemie, Ruhr-Universität Bochum, 44780 Bochum, Germany*

[a)] *Present address: Yusuf Hamied Department of Chemistry, University of Cambridge, Cambridge, CB2 1EW, UK*

[b)] *Present address: Laboratoire Matière en Conditions Extrêmes, Université Paris-Saclay, CEA, DAM, DIF, 91297 Arpajon, France*

(Dated: June 22, 2022)

CONTENTS

I. BENCHMARKING THE ELECTRONIC STRUCTURE METHOD

The choice of the electronic structure method is an important ingredient in the quality of any generation of parametrized potential energy functions, including the presented data-driven methodology. Here, it will define the ultimate accuracy limit that can be achieved with the interaction neural network potentials (NNPs), both the all-atom and the AHR-averaged ones, independently from the quality of the fits as such. In our previous work [1], where the interaction potential between a solute molecule and helium has been obtained in the framework of NNPs as reviewed recently [2], it has been demonstrated that essentially converged coupled cluster electronic structure calculations [3–5] can be used – in practice – in order to parametrize interaction NNPs at this quality level in a fully data-driven approach. Therein, the interaction energies have been computed using single, double and scaled perturbative triple excitations CCSD(T*), broadly considered the 'gold standard' in quantum chemistry, in conjunction with using the F12a explicit correlation factor in the wavefunction [6, 7] together with the aug-cc-pVTZ basis set [8, 9], as well as the counterpoise (cp) correction [10] considering the two interacting species has been applied in order to correct for the basis set superposition error, dubbed CCSD(T*)-F12a/aVTZcp method also abbreviated by 'CC' in the present context. We have explicitly shown previously [1], for the case of He interactions with protonated water clusters from the hydronium cation to larger ones, that the combination of the F12a technique together with the cp correction yields essentially converged CCSD(T*) interaction energies using that aug-cc-pVTZ triple-zeta basis set to expand the orbitals. This is documented in Section I.A of the Supplemental Material of Ref. 1 by explicit statistical comparison of CCSD(T*)-F12a/aVTZcp and CCSD(T*)-F12a/aVQZcp data to the results obtained in the complete basis set (CBS) limit, CCSD(T*)/CBS. Although we therefore know that the CCSD(T*)-F12a/aVTZcp method shows excellent performance for computing the interaction energies between solute molecules and helium, additional benchmark calculations have been performed in order to ensure that this method provides practically converged results also in the case of interactions with H_2.

The electronic structure method has been benchmarked, both for the $H_2O\cdots H_2$ and $H_3O^+\cdots H_2$ interactions, using many different orientations of the H_2 molecule with respect to the solute while scanning distances. Thus, we validate here the underlying electronic structure method by directly comparing full potential energy profiles along relevant coordinates, thereby transcending our previous purely statistical assessment [1]. For simplicity, only two of them for the $H_2O\cdots H_2$ interaction are shown here since they are representative, see Figure 1. The electronic structure methods used are the CCSD(T*)/aVTZcp, CCSD(T*)-F12a/aVTZcp,

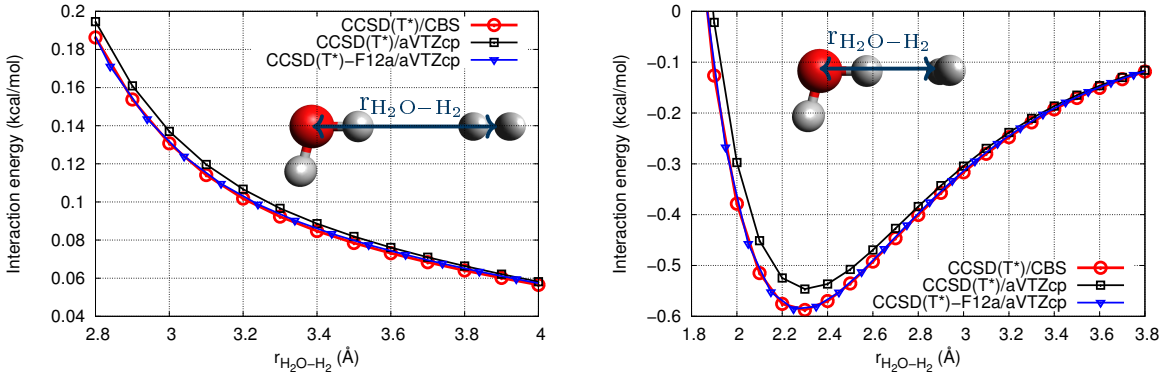

FIG. 1. Results of the benchmark calculations for the $H_2O\cdots H_2$ interaction for different CC methods and basis sets, see text. The orientation of the molecules is given as an inset, one of them having the H_2 molecule aligned with the O-H bond (left), whereas the other one has the H_2 oriented at 90° with respect to the same O-H bond (right).

and CCSD(T*)/aVQZcp methods, from which the CBS limit CCSD(T*)/CBS has been calculated following our earlier work [1]. As before, all interaction energies have been computed in the present investigation using the `Molpro` program [11, 12].

The results for two important orientations of the $H_2O\cdots H_2$ complex are presented in Figure 1. In both cases, the F12a explicit correlation factor in conjunction with using the aVTZ basis and the cp correction provides us with reference interaction energies for the NNP generation that are indistinguishable – on the relevant energy scale – from the CBS data. This analysis also makes clear that this perfect agreement with the numerically exact CCSD(T*) energies can only be achieved thanks to using the F12a factor in the expansion of the many-body wavefunction in terms of the orbitals when using that triple-zeta basis set while the traditional CCSD(T*)/aVTZcp method (also including the cp correction) consistently over/underestimates the repulsive/attractive interactions as seen in the left/right panels. Very similar results, therefore not presented, have also been found for the interaction energies in other arrangements of $H_2O\cdots H_2$ as well as of $H_3O^+\cdots H_2$. The conclusion of our benchmarking is that the (non-CBS-extrapolated) CCSD(T*)-F12a/aVTZcp interaction energies provide converged CC reference data to which the interaction NNPs will be fitted, thus avoiding explicit extrapolation based on multiple basis set calculations for each configuration in the reference data set. Therefore, the CCSD(T*)-F12a method together with the aug-cc-pVTZ basis set and the counterpoise correction is used to describe the *impurity*$\cdots H_2$ interactions.

Last but not least, it is important to point out that the interaction energies for one of the orientations shown in Figure 1 are repulsive for the whole range of distances (left), whereas

the other orientation (right) shows an attractive minimum. This gives an indication on how anisotropic the potential is, as a change in the orientation of the H_2 molecule by 90° results in a change from the repulsive regime to a minimum in the potential energy surface of about 0.6 kcal/mol at a distance of 2.8 Å and increases even more at smaller distances (not shown). An example of this would be at a distance of 2.3 Å, where the interaction energy for the scans in the left and right panels of Figure 1 are about 0.7 and -0.6 kcal/mol respectively, adding up to a total difference of 1.3 kcal/mol for a rotation of the H_2 molecule that amounts to 90°. Such energy changes are not only very relevant on the scale of the maximum interaction energy between two pH$_2$ molecules of ≈ 0.07 kcal/mol (according to the Silvera-Goldman effective pair potential [13]), but also significantly affect the adiabatic hindered rotor (AHR) averaging in large regions of the intermolecular configuration space. Therefore, the use of the AHR-averaging approximation to go beyond the standard spherical average of the interaction potential is of great importance. In the AHR-averaging context, it is also reassuring to infer from Figure 1 that the CCSD(T*)-F12a/aVTZcp used here throughout performs consistently well compared to the CBS benchmark to quantify both, repulsive and attractive interaction energies at the same intermolecular distance.

II. ALL-ATOM $H_2O\cdots H_2$ INTERACTION NNP

The two all-atom NNPs that have been generated for the two solute molecules as explained in the main text need to be carefully tested with special emphasis on accurately describing – at the level of that interim NNP – the rotation of the two-site H_2 molecule around its center of mass. This is especially important because the AHR-averaging procedure requires interaction energies for very many different orientations of the H_2 molecule and the accuracy on those interaction energies – as described by the all-atom NNP – will translate to that of the final AHR-averaged NNP. The easiest testing of the accuracy of the all-atom fits is a direct comparison between the reference electronic structure method, CCSD(T*)-F12a/aVTZcp here, and the predicted interaction enegies from the generated all-atom NNP. This has been performed for several scans along the interaction potential energy surface, namely radial, angular and also two-dimensional cuts, see Figures 2 to 5.

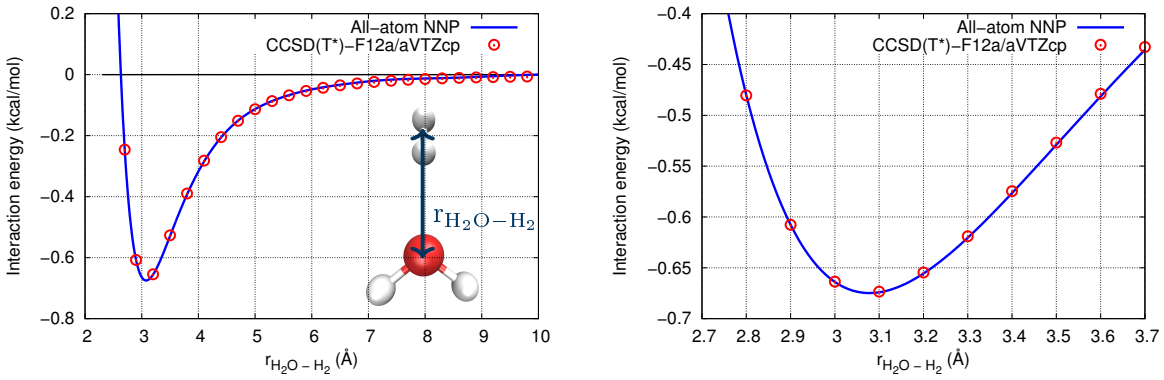

FIG. 2. Comparison between the interaction energies computed with the reference CCSD(T*)-F12a/aVTZcp method (symbols mark these single-point numerical data here and in subsequent such plots) and the all-atom NNP (solid line marks these continuous analytical data here and in subsequent such plots) for the radial scan along the C_{2v} axis of the water molecule with H_2 in the same plane as the H_2O molecule (see inset). The right panel magnifies the region around the minimum of the interaction energy profile.

First, a radial scan for a frozen structure of the water molecule and fixed orientation of the H_2 molecule is shown in Figure 2. It can be observed that the quality of the all-atom NNP along this scan is almost perfect when compared to the explicit single-point reference electronic structure calculations. Similar accuracy is found in Figure 3, where the reference CC interaction energies and the energies computed from the all-atom NNP are compared for four different angular scans of $H_2O\cdots H_2$. These scans correspond to two different arrangements of the system in the

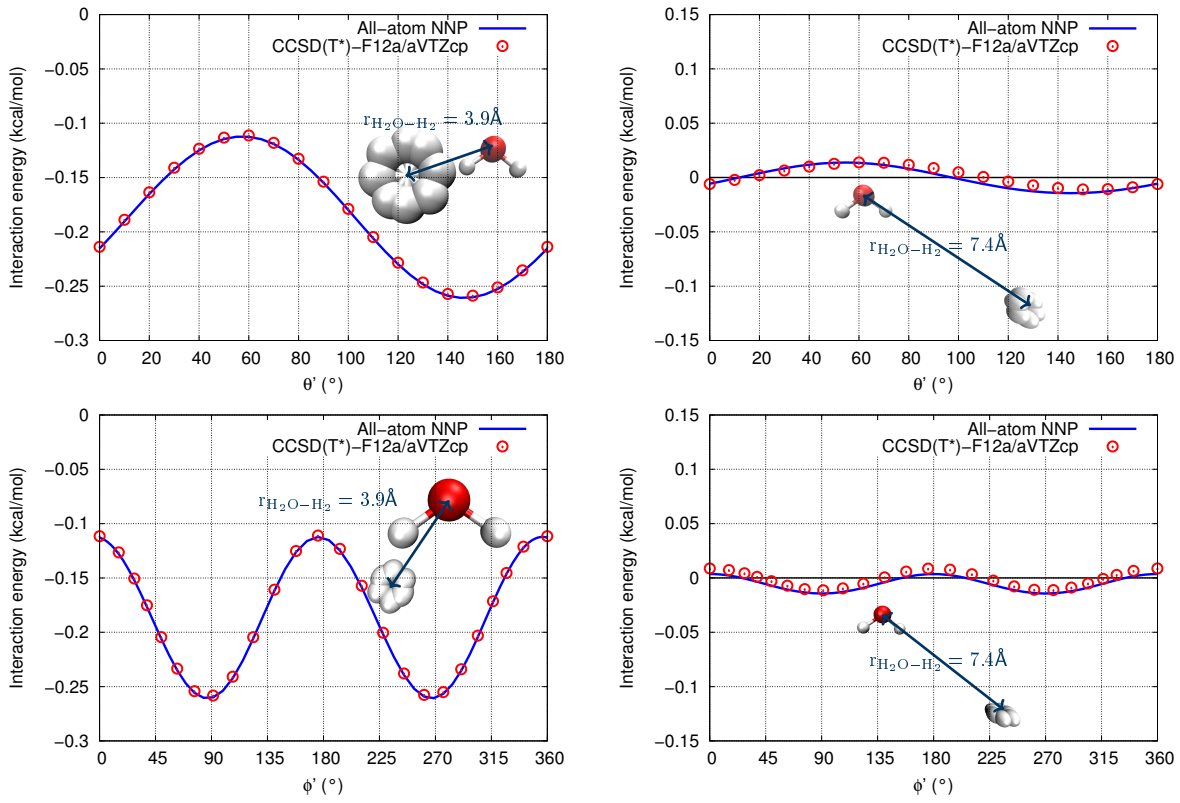

FIG. 3. Comparison between the interaction energies computed with the reference CCSD(T*)-F12a/aVTZcp method and the all-atom NNP for two different conformations of the $H_2O\cdots H_2$ system (left and right) as a function of the rotation of the H_2 molecule around its center of mass along the θ' (top) and ϕ' (bottom) angles.

left and right panels as depicted in the insets, while the rotation is performed w.r.t. different angles, namely along the θ' and ϕ' angles in the top and bottom panels, respectively. These one-dimensional interaction energy profiles already give a hint of the favorable accuracy of the all-atom interaction NNP for the rotation of the H_2 molecule around its center of mass, but a more stringent benchmark is provided by two-dimensional cuts through the corresponding potential energy surface as follows.

Thus, two-dimensional cuts of the interaction potential energy surface have been scrutinized. One of them has a fixed distance between the H_2O and the H_2 molecules as well as a fixed orientation of the H_2 molecule with respect to its center of mass whereas the relative orientation between the two molecules is changed (see Figure 4). The second one has a fixed position of the H_2 center of mass with respect to the water molecule whereas the orientation of the H_2 molecule is varied (see Figure 5). In both cases, the comparison between the interaction energies is shown by superimposing contour plots. The agreement found between the CC refer-

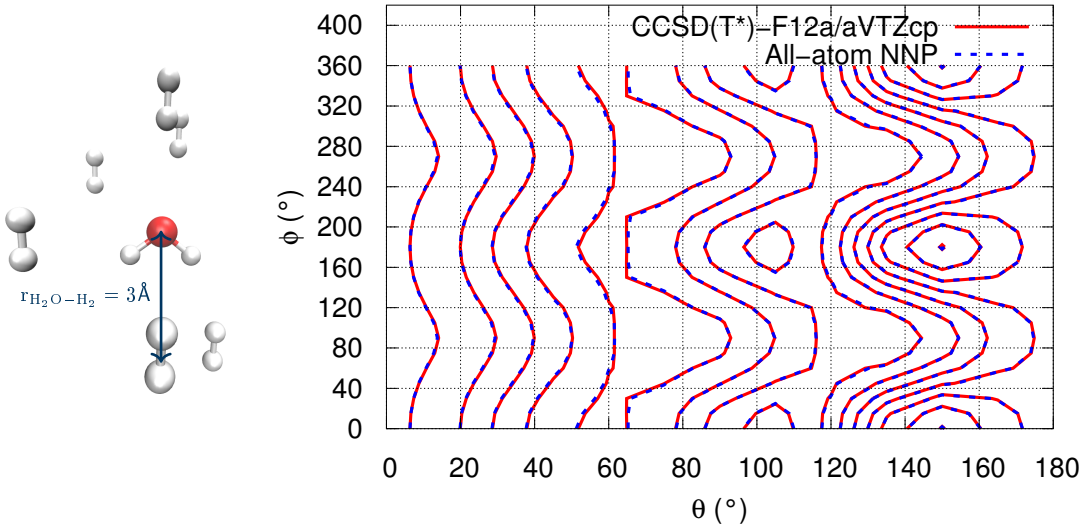

FIG. 4. Comparison of the contour plots obtained with the all-atom NNP interaction energies and the CCSD(T*)-F12a/aVTZcp interaction energies for a two-dimensional scan over the orientation of the H_2 molecule around the H_2O molecule at the global minimum energy structure, where the orientation of H_2 with respect to its center of mass is kept fixed. The energy scale corresponding to this contour plot is −3.0 to 5.0 kcal/mol.

ence and the all-atom NNP interaction energies is almost perfect. The favorable comparisons of these two-dimensional scans are very significant, since they show that the loss of accuracy when performing the AHR average using the all-atom interaction NNP will be minimal when compared to the computationally very demanding CCSD(T*)-F12a/aVTZcp method. This almost perfect accuracy is mandatory since the all-atom interaction NNP is used in the subsequent step to perform the AHR averages that yield the reference energies to parametrize the AHR-averaged interaction NNP, thus allowing for an efficient evaluation of the AHR-averaged energies at the CC level of accuracy but without the need of performing hundreds of thousands of the computationally very demanding CC calculations to obtain the AHR-averaged interaction NNP; recall that in order to compute each of the AHR reference energies, $64 \times 32 = 2048$ interaction energies are needed, making the direct generation of the AHR-averaged NNP using explicit CCSD(T*)-F12a/aVTZcp calculations to evaluate each of them computationally too expensive given that around 60 000 AHR energies are needed to parametrize the AHR-averaged interaction NNP which includes here the full flexibility of the solute.

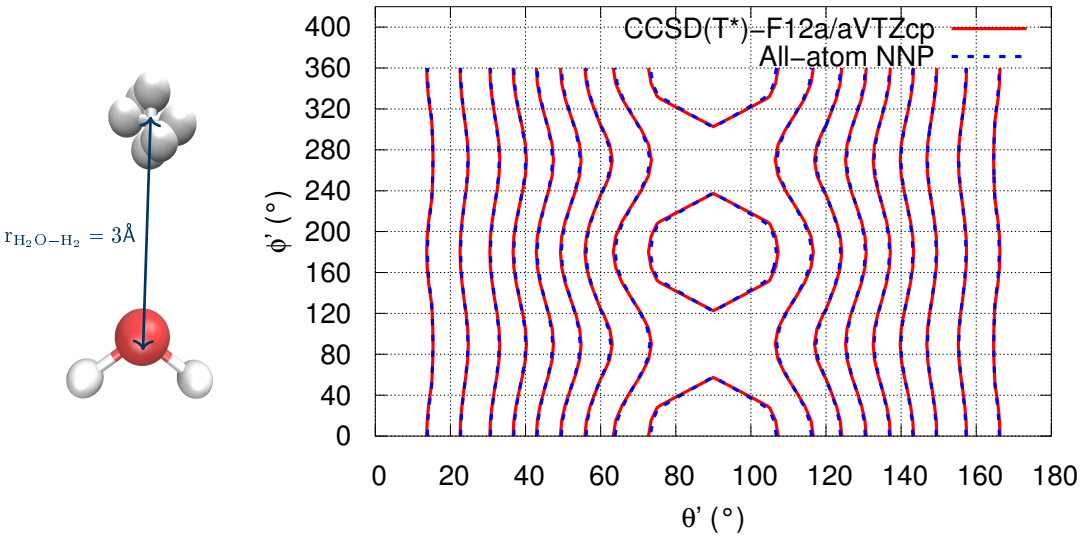

FIG. 5. Comparison of the contour plots obtained with the all-atom NNP interaction energies and the CCSD(T*)-F12a/aVTZcp interaction energies for a two-dimensional scan over the orientation of the H_2 molecule around its center of mass, with the H_2O molecule at the global minimum energy structure keeping the H_2 center of mass fixed. The energy scale corresponding to this contour plot is −3.0 to 1.5 kcal/mol.

III. AHR-AVERAGED POTENTIAL ENERGY CONVERGENCE

In order compute the AHR-averaged interaction potential energies $V^{\mathrm{AHR}}(R,\theta,\phi)$, the adiabatic Schrödinger equation given by Eq. (1) in the main text needs to be solved for the lowest energy eigenvalue which provides V^{AHR} at the point (R,θ,ϕ) that specifies the intermolecular configuration; see the middle panel of Figure 1 in the main text for the definition of these spherical coordinates. Solving this equation requires, on one side, the use of a linear combination of spherical harmonics up to a maximum l_{max} given by Eq. (2) in the main text. On the other side, the evaluation of the potential energy contribution requires a numerical integration using Gauss-Legendre and Gauss-Chebyshev quadrature points to average over the θ' and ϕ' angles, respectively, according to Eq. (3) in the main text. The l_{max} parameter as well as the number of Gauss-Legendre and Gauss-Chebyshev quadrature points need to be determined beforehand, making sure that the obtained AHR-energy is converged while not wasting computer time since the matrix elements $\langle Y_{l'}^{m'}|V(R,\theta,\phi,\theta',\phi')|Y_l^m\rangle$ need to be evaluated extremely often to implement the AHR-averaging procedure based on the underlying all-atom interaction potential V that is represented in its turn by a corresponding all-atom interaction NNP.

The convergence tests for these parameters have been performed using different configurations of both, $H_2O\cdots pH_2$ and $H_3O^+\cdots pH_2$ but for simplicity only the results obtained for H_2O is its minimum energy structure and the center of mass of pH_2 at a distance $R = 3.3$ Å and angles $\theta = 180°$ and $\phi = 0°$ according to the coordinates defined in the central panel of Figure 1 in the main text are reported here. In this section, the AHR-averaged interaction energies have been computed with the all-atom NNP and also with the explicit reference method, where lots of CCSD(T*)-F12a/aVTZcp single-point calculations for many different H_2 orientations are required to compute the all-atom matrix elements $\langle Y_{l'}^{m'}|V(R,\theta,\phi,\theta',\phi')|Y_l^m\rangle$. First, the number of Gauss-Legendre and Gauss-Chebyshev quadrature points have been increased progressively from 2 and 4 to 128 and 256, respectively, while fixing $l_{\mathrm{max}} = 8$. Here it is important to point out that the number of Gauss-Chebyshev quadrature points is always twice the number of Gauss-Legendre quadrature points, as the ϕ' interval is two times larger than the θ' interval, and this ensures that the angular bin size remains the same for the two angles.

The convergence of the AHR-averaged energies with the number of quadrature points for the integration of the potential matrix elements is shown in Figure 6 (left), where it is possible to see that using 10 to 12 Gauss-Legendre and 20 to 24 Gauss-Chebyshev quadrature points yields converged energies on the relevant scale. Similarly, the percentage of spherical character of the structure is studied. This percentage indicates how important the contribution of the spherical state (i.e. $l = 0$ and thus $m = 0$) to the adiabatic hindered rotor average is. The

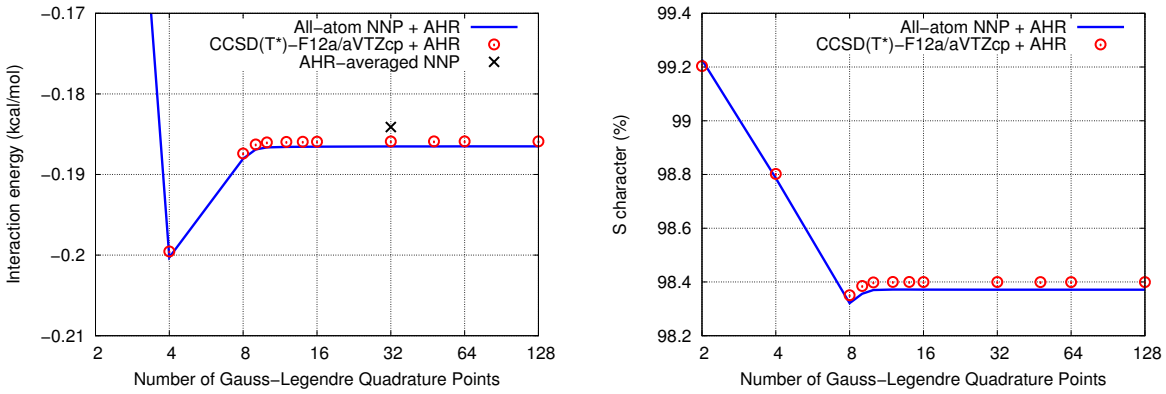

FIG. 6. Convergence study of the AHR-averaged energy (left) and the spherical character in percent (right) for $H_2O\cdots pH_2$ in the AHR minimum structure, see text, as a function of the number of Gauss-Chebyshev and Gauss-Legendre quadrature points used for the integration of the interaction potential energy matrix elements with respect to ϕ' and θ', respectively, whereas l_{max} is set to 8. The black cross marks the interaction energy as directly obtained from the AHR-averaged NNP at the accuracy level used to generate it. For simplicity, only the number of number of Gauss-Legendre quadrature points are reported in the axis of the graph, but the number of Gauss-Chebyshev quadrature points is indirectly provided since is it twice the number of Gauss-Legendre quadrature points, see text. Note that the blue line connecting the points of the all-atom NNP + AHR averaging is a guide to the eye.

smaller it is, the larger is the contribution of $l > 0$ states and thus the more pronounced is the influence of anisotropy within the AHR-averaged energy. In other words, the smaller the s-character the larger is the systematic error made when the simple spherical $l_{\max} = 0$ average is used to produce the effective interaction energy of the single-site pH_2 point particle from all-atom H_2. The results are shown on Figure 6 (right), and also for this property only $10 - 12$ Gauss-Legendre and $20 - 24$ Gauss-Chebyshev quadrature points suffice to compute the converged value.

As already mentioned, the same convergence study has been performed for other $H_2O\cdots H_2$ and $H_3O^+\cdots H_2$ configurations and it has been found that those structures with slightly repulsive AHR-averaged energies require a larger number of quadrature points to achieve convergence, namely 32 and 64 quadrature points for Gauss-Legendre and Gauss-Chebyshev, respectively. Those structures also have a smaller s-character, meaning that the $l > 0$ states and thus anisotropies contribute more to the AHR-averaged energies. Indeed, they feature a higher anisotropy on the all-atom potential energy surface when performing rotations of the H_2 molecule around its center of mass, which explains why more quadrature points are necessary in order to get a converged AHR-averaged interaction potential energy.

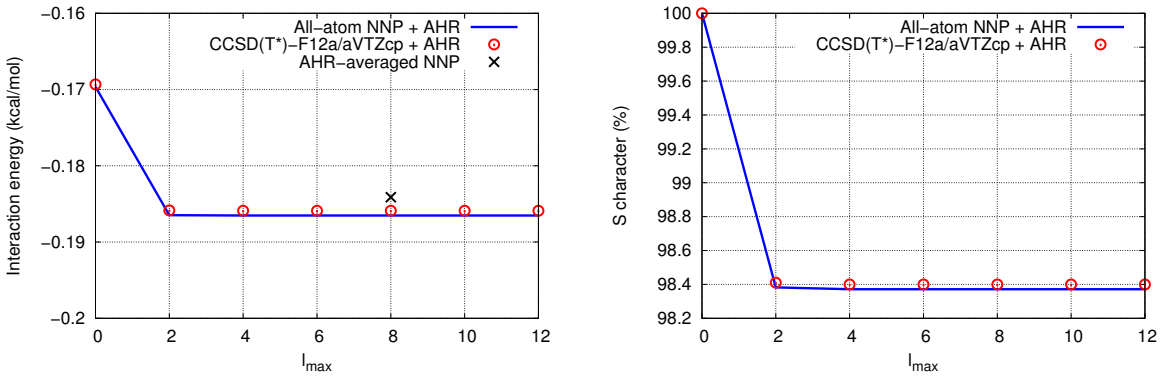

FIG. 7. Convergence study of the AHR-averaged energy (left) and the spherical character in percent (right) for $H_2O\cdots pH_2$ in the AHR minimum structure, see text, as a function of $l_{\max}$ used in the basis set expansion according to Eq. (2) in the main text, whereas the number of Gauss-Legendre and Gauss-Chebyshev quadrature points are set to 32 and 64, respectively. The black cross marks the interaction energy as directly obtained from the AHR-averaged NNP at the accuracy level used to generate it. Note that the blue line connecting the points of the all-atom NNP + AHR averaging is a guide to the eye.

After that, we carried out a second convergence study to determine $l_{\max}$, fixing the number of Gauss-Legendre quadrature points to 32 and the Gauss-Chebyshev quadrature points to 64, while now increasing l_{max} from 0 to 12 in steps of 2 (together with using all corresponding m quantum numbers). Note that since we are considering pH_2 here, the AHR-average only includes even l states. The results obtained for the energy and the spherical character are presented in Figure 7. In this case, $l_{\max} = 2$ includes almost all the anisotropy of the structure, but going up to $l_{\max} = 4$ is required to reach full convergence. It needs to be taken into account, though, that this structure has an s-character on the order of 98.4% and, therefore, is not highly anisotropic. Similarly to the number of quadrature points, the $l_{\max}$ convergence has also been tested with other structures, and those with a lower s-character require up to $l_{\max} = 8$ to reach convergence. Therefore, unless otherwise reported, all the AHR-averaged energies are computed using $l_{\max} = 8$ in conjunction with 32 Gauss-Legendre and 64 Gauss-Chebyshev quadrature points.

Finally, Figures 6 and 7 not only report the AHR-averaged energy computed from the all-atom interaction NNP and the CCSD(T*)-F12a/aVTZcp method, but also the interaction energy that is directly predicted by the AHR-averaged NNP using the converged l_{max} and quadrature point parameters, see the black crosses. Therefore, this is a good estimate of the overall accuracy of the methodology presented in this paper. For this particular structure, the

difference between the AHR-averaged NNP interaction energy and the AHR-averaged energies computed from CC or from the all-atom interaction NNP is of the order of 0.002 kcal/mol.

IV. AHR-AVERAGED $H_2O\cdots pH_2$ INTERACTION NNP

The next step in our data-driven procedure consists in generating the AHR-averaged interaction NNPs. The accuracy of these AHR-averaged NNP has been tested by explicitly comparing the obtained AHR-averaged interaction energies from the AHR-averaged NNP to the interaction energies obtained while performing explicitly the AHR average using the all-atom NNP along different radial, angular and two-dimensional cuts of the respective potential energy surface. It could not be tested against the AHR-energies obtained with the electronic structure CC method underlying the all-atom NNP due to the outrageous computational effort that would be involved to carry out these CCSD(T*)-F12a/aVTZcp calculations as discussed in detail in the main text. Note that the AHR average of the all-atom NNP is performed using the same $l_{\max}$ and number of Gauss-Legendre and Gauss-Chebyshev quadrature points as when generating the AHR-averaged NNP itself, namely 8, 32 and 64, respectively.

The result for the radial scan along the C_{2v} axis of the water molecule is shown in Figure 8 (left), and an angular scan (at the fixed intermolecular distance as indicated in the inset) is shown in the same figure in the right panel. In both cases the agreement between the AHR-interaction energy computed from the all-atom NNP after explicit AHR averaging and that predicted with the AHR-averaged NNP is almost perfect in particular considering the energy scales. A similar but now two-dimensional angular cut along the potential energy surface is shown in Figure 9, where a very good accuracy can again be observed.

Last but not least, we report the computed spatial distribution functions (SDFs) from bosonic path integral simulations at a temperature of 1 K for $H_2O(pH_2)_N$ complexes with $N = 1, 3, 8$ and 18 pH_2 in Figure 10. Similarly to the main text, the SDFs are computed on a grid for a H_2O molecule fixed at its minimum energy structure using (i) the reference CC method and performing the AHR-average on the obtained energies, (ii) performing the AHR-average while using the all-atom NNP interaction energies, (iii) directly using the AHR-averaged NNP, and (iv) using the published AHR-averaged potential from Ref. 14. Overall, there are no significant deviations between the SDFs obtained with the four different methods, in agreement with the rest of the cluster sizes presented in the main text.

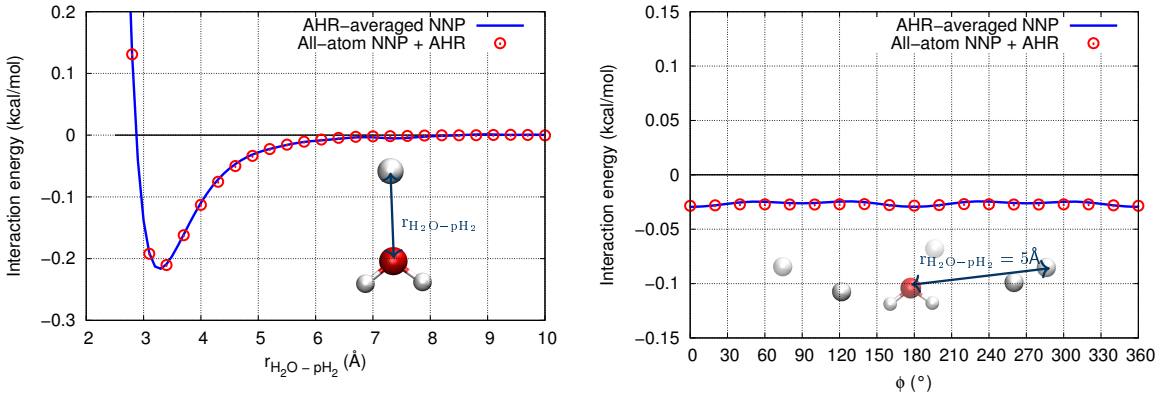

FIG. 8. Comparison between the AHR-averaged interaction energies obtained with the AHR-averaged NNP and performing the AHR average with the all-atom NNP for a radial (left) and an angular (right) cut of the $H_2O\cdots pH_2$ system. The configurations used for these cuts are provided in the insets.

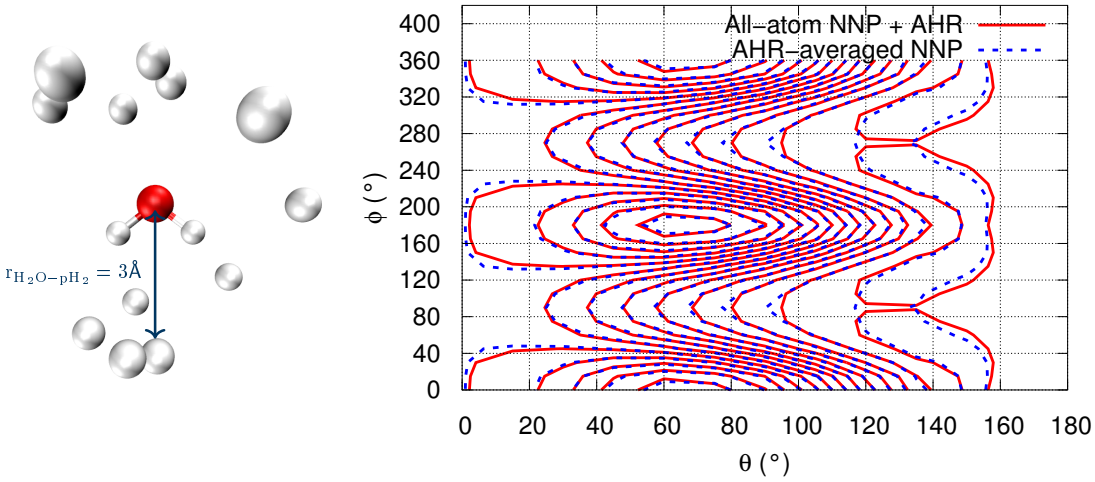

FIG. 9. Comparison of the contour plots obtained with the AHR-averaged interaction energies obtained with the AHR-averaged NNP and performing the AHR average using the all-atom NNP for a two-dimensional angular scan of the $H_2O\cdots pH_2$ system. The configuration used for this scan is provided in the left panel and energy scale corresponding to this contour plot ranges from -0.25 to 0.05 kcal/mol.

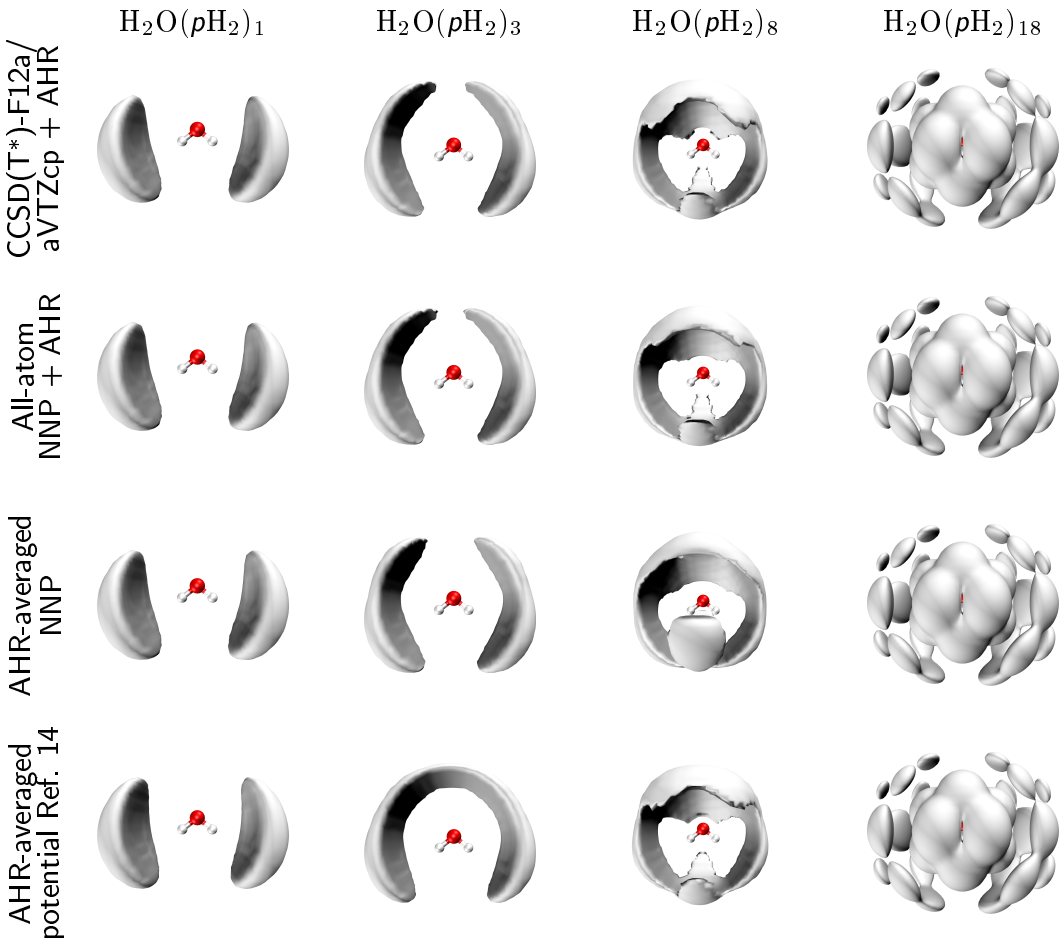

FIG. 10. Comparison of the pH_2 SDFs around frozen H_2O on a grid, see text, obtained with different methods to compute the interactions for four cluster sizes N. From top to bottom: (i) CCSD(T*)-F12a/aVTZcp + AHR-averaging, (ii) all-atom $H_2O\cdots pH_2$ NNP + AHR averaging, (iii) AHR-averaged $H_2O\cdots pH_2$ NNP, and (iv) AHR-averaged potential from Ref. 14. From left to right: $N = 1$, 3, 8 and 18 pH_2 molecules solvating the minimum energy structure of the water molecule. The isovalues are 0.0009, 0.0038, 0.0075, and 0.0015 1/bohr^3 for $N = 1$, 3, 8 and 18.

V. ALL-ATOM $H_3O^+ \cdots H_2$ INTERACTION NNP

The methodology presented in this paper as detailed herein so far for H_2O has also been applied to generate the all-atom and AHR-averaged interaction NNPs to describe the $H_3O^+ \cdots pH_2$ interaction. Therefore, in this and the following sections, we will validate the accuracy of the obtained interaction NNPs for the hydronium cation.

In the first step, the all-atom NNP is generated where the rotational degrees of freedom of H_2 are included explicitly. This all-atom $H_3O^+ \cdots H_2$ interaction NNP has been carefully tested by explicitly comparing the energies predicted by the all-atom NNP to the reference CCSD(T*)-F12a/aVTZcp calculations for some cuts along the potential energy surface. Such an approach is limited to small sections of the configuration space and it is therefore complementary to the more meaningful and complex testing shown in the main text using SDFs computed from path integral simulations. We want to highlight that the main focus of this testing is on the rotation of the H_2 molecule around its center of mass given a configuration of the H_3O^+ solute, as this is very important for the AHR averaging procedure and will ultimately limit how accurate this averaging can be.

The results for a radial scan are given in Figure 11. On the relevant scale of the interaction potential energy surface (left panel) it is found that essentially no differences between the all-atom NNP and the CC interaction energies can be seen. However, slight differences between the CC and the all-atom NNP are observed in the zoom-in that is depicted in the right panel. These small deviations are about 0.015 kcal/mol and, thus, are considered negligible on the relevant energy landscape. A similar comparison has also been carried out for scans along the rotational degrees of freedom: Figure 12 shows the results for two of them, one for the rotation of the center of mass of the H_2 molecule around H_3O^+ (left panel) and another one for the rotation of the H_2 molecule around its center of mass (right panel); the same coordinate system as introduced in the middle panel of Figure 1 in the main text is used. Both of them show a convincing agreement between the interaction energies predicted with the all-atom NNP and those computed explicitly with the CCSD(T*)-F12a/aVTZcp reference method.

Finally, also two-dimensional cuts of the potential energy surface have been analyzed for the H_3O^+ case. Figure 13 illustrates the quality of the fit when changing the orientation of the H_2 molecule around the H_3O^+ molecule but keeping fixed the orientation of the H_2 around its center of mass, whereas Figure 14 shows the opposite, i.e. the H_2 molecule rotates around its center of mass and this one has a fixed orientation with respect to the H_3O^+ molecule. But in both cases, the agreement between the all-atom interaction NNP and the CC reference method is almost perfect.

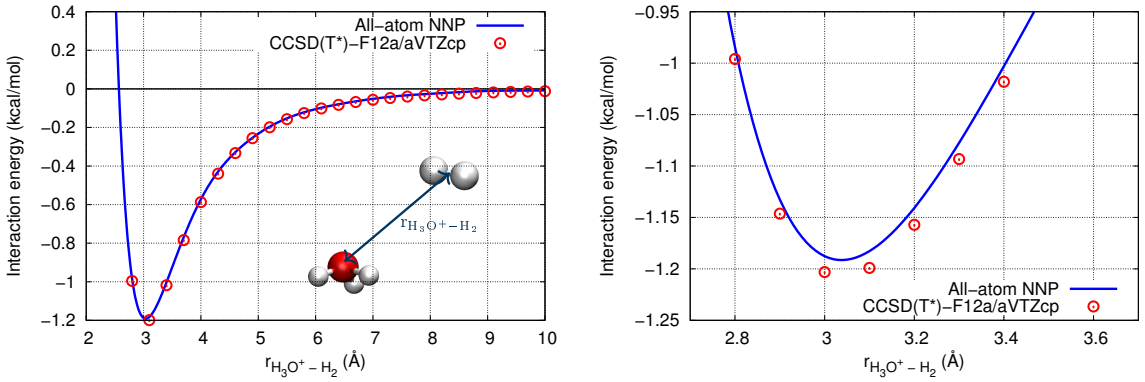

FIG. 11. Comparison between the interaction energies computed with the reference CCSD(T*)-F12a/aVTZcp method and the all-atom NNP for a radial scan of H_3O^+-H_2 (see inset). The right panel magnifies the region around the minimum of the interaction energy profile.

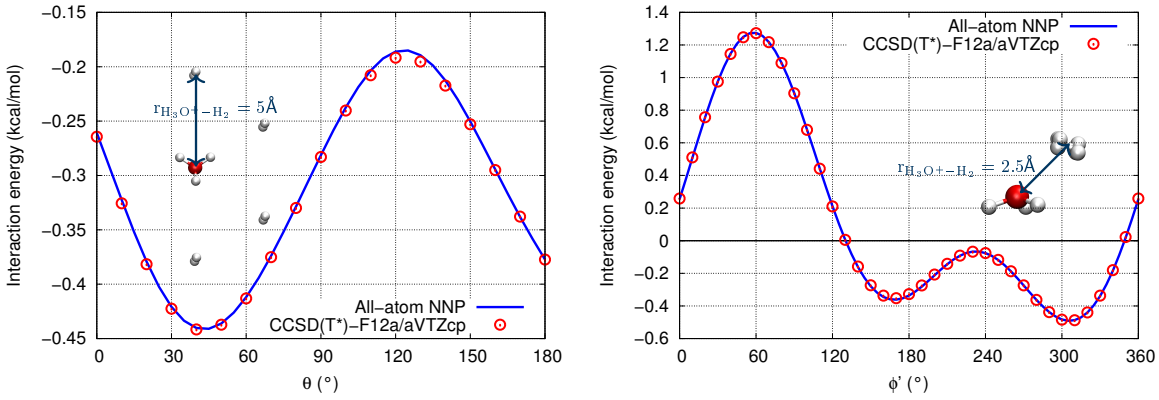

FIG. 12. Comparison between the interaction energies computed with the reference CCSD(T*)-F12a/aVTZcp method and the all-atom NNP for two different conformations of the $H_3O^+\cdots H_2$ system (left and right) as a function of the rotation of the center of mass of the H_2 molecule around the H_3O^+ molecule along the θ angle (left) and the rotation of the H_2 molecule around its center of mass along the ϕ' angle (right).

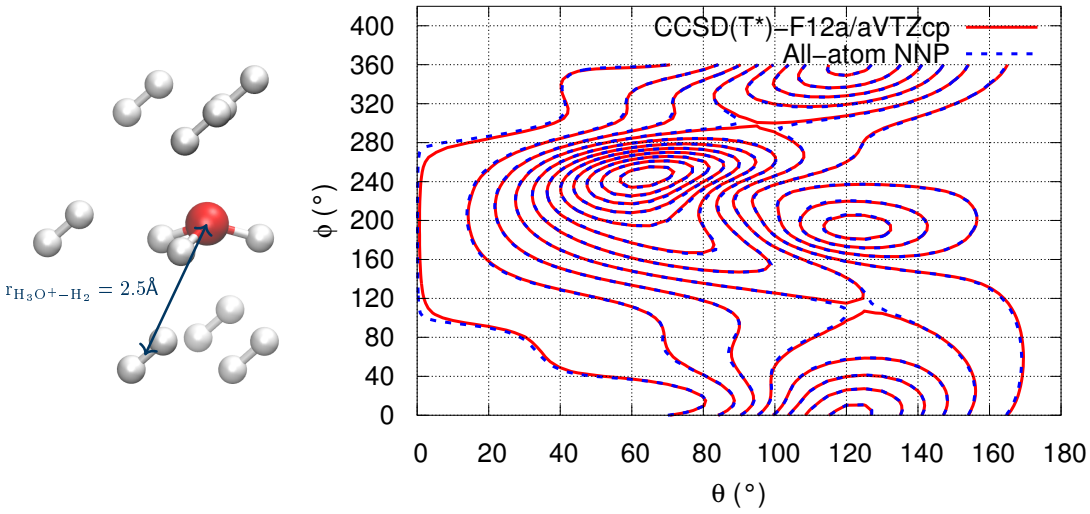

FIG. 13. Comparison of the contour plots obtained with the all-atom NNP interaction energies and the CCSD(T*)-F12a/aVTZcp interaction energies for a 2-dimensional scan over the orientation of the H_2 molecule around the H_3O^+ molecule at the global minimum energy structure, where the orientation of H_2 with respect to its center of mass is kept fixed. The energy scale corresponding to this contour plot is -10 to 4 kcal/mol.

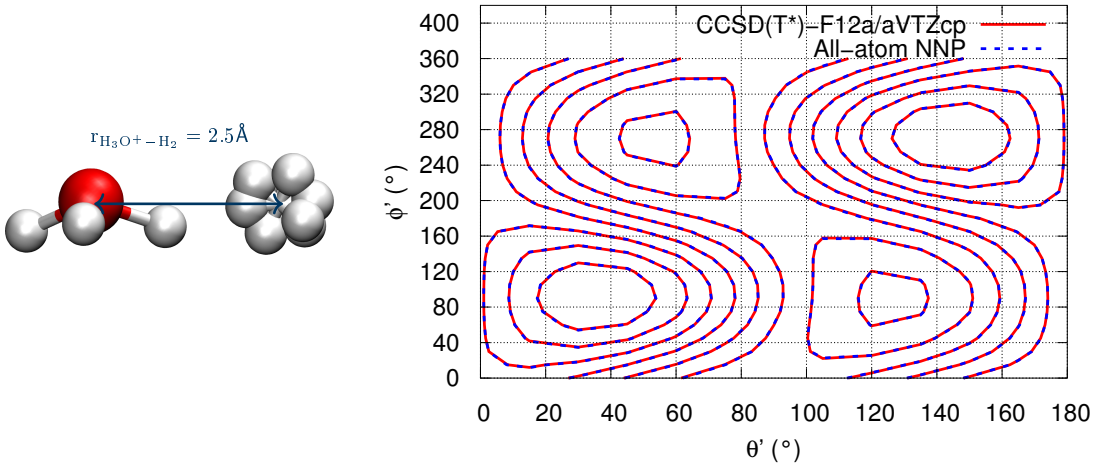

FIG. 14. Comparison of the contour plots obtained with the all-atom NNP interaction energies and the CCSD(T*)-F12a/aVTZcp interaction energies for a 2-dimensional scan over the orientation of the H_2 molecule around its center of mass, with the H_3O^+ molecule at the global minimum energy structure keeping the H_2 center of mass fixed. The energy scale corresponding to this contour plot is -3 to 1.5 kcal/mol.

VI. AHR-AVERAGED $H_3O^+ \cdots pH_2$ INTERACTION NNP

As for water, the all-atom NNP generated to describe the $H_3O^+ \cdots H_2$ interaction can be used to obtain the AHR-averaged NNP. In order to test the accuracy of the AHR-averaged network, an explicit comparison between the interaction energies predicted by the AHR-averaged NNP and the AHR-averaged energies computed from the all-atom NNP is performed for the hydronium cation. Again, the AHR interaction energies are computed using the same number of quadrature points and $l_{\max}$ that have been used to generate the AHR-averaged NNP, so 32 Gauss-Legendre and 64 Gauss-Chebyshev quadrature points together with $l_{\max} = 8$.

The results of these tests of the AHR-averaged NNP are shown in Figure 15 as radial (left panel) and angular (right) scans and in Figure 16 as a two-dimensional scan in the two angular degrees of freedom using the coordinate system from the middle panel of Figure 1 in the main text and the configurations depicted in these figures. In all three representative cases, the agreement between the averaged energies predicted by the AHR-averaged NNP and those computed by performing the explicit AHR-average with the all-atom NNP is almost exact.

Also for H_3O^+ we report in Figure 17 the obtained SDFs for the $H_3O^+(pH_2)_N$ clusters for $N = 1,\ 3,\ 8$ and 18 pH_2 from left to right. The SDFs are computed on a grid keeping the H_3O^+ molecule fixed according to its minimum energy structure using (i) the CC reference method and performing the AHR-average on the obtained energies (top row), (ii) performing the AHR-average using the all-atom NNP interaction energies (middle row), and (iii) using directly the final AHR-averaged interaction NNP (bottom row). Overall, there are no significant deviations between the SDFs of pH_2 around H_3O^+ obtained with the three different methods in agreement with the other the cluster sizes presented on the main text.

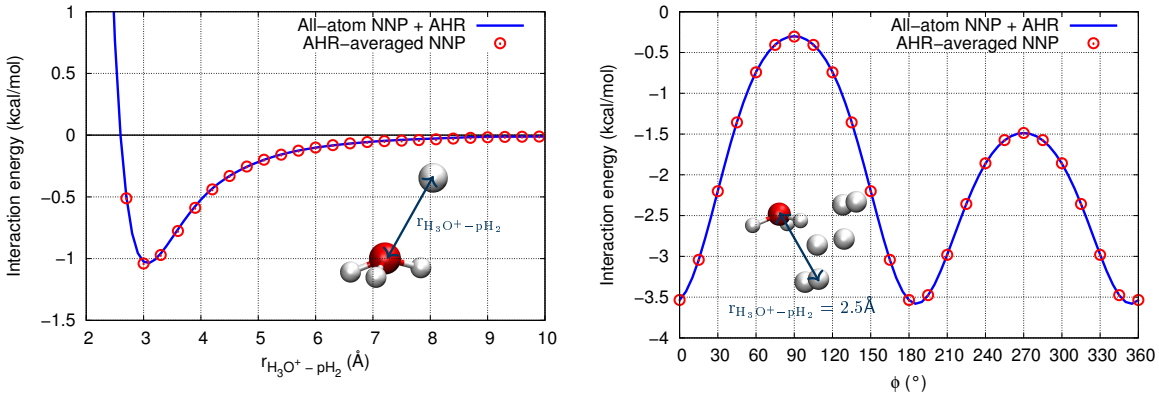

FIG. 15. Comparison between the AHR-averaged interaction energies obtained with the AHR-averaged NNP and performing the AHR-average with the all-atom NNP for a radial (left) and an angular scan (right) of the $H_3O^+ \cdots pH_2$ system. The configurations used for these scans are provided in the insets.

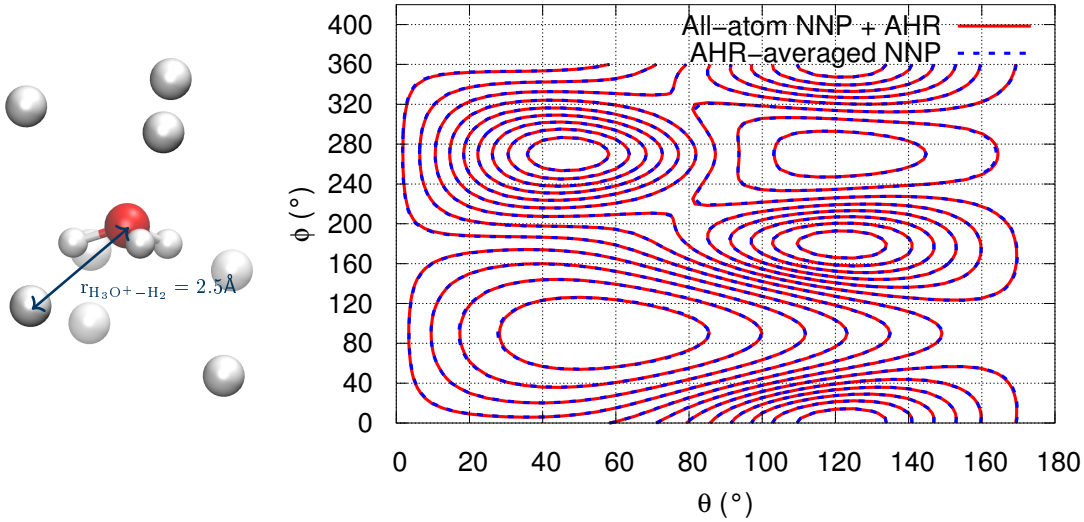

FIG. 16. Comparison of the contour plots obtained with the AHR-averaged interaction energies obtained with the AHR-averaged NNP and performing the AHR average using the all-atom NNP for a 2-dimensional angular scan of the $H_3O^+ \cdots pH_2$ system. The configuration used for this scan is provided in the left panel and the energy scale corresponding to this contour plot ranges from -4 to 0 kcal/mol.

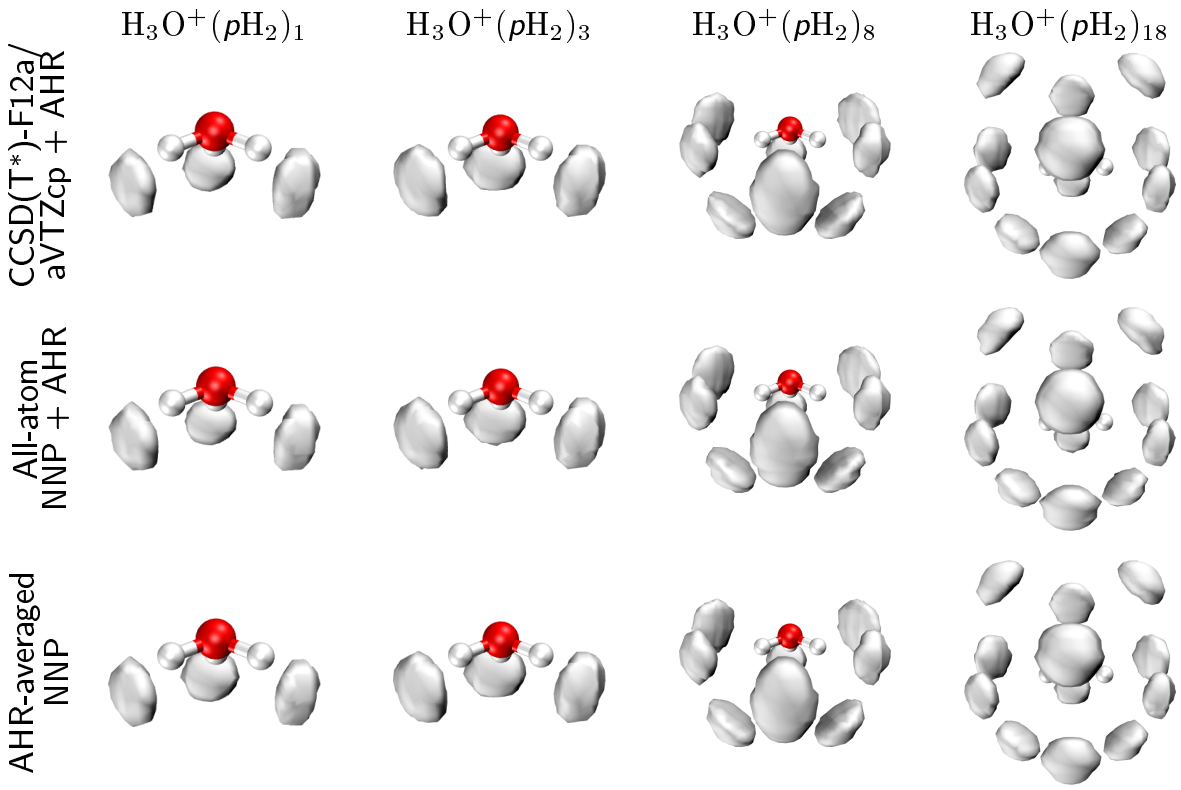

FIG. 17. Comparison of the pH_2 SDFs around frozen H_3O^+ on a grid, see text, obtained with different methods to compute the interactions for four cluster sizes N. From top to bottom: (i) CCSD(T*)-F12a/aVTZcp + AHR averaging, (ii) all-atom $H_3O^+\cdots H_2$ NNP + AHR averaging, and (iii) AHR-averaged $H_3O^+\cdots pH_2$ NNP. From left to right: $N = 1$, 3, 8 and 18 pH_2 molecules solvating the minimum energy structure of the hydronium cation. The isovalues are 0.0250 for $N = 1$, 3 and 8 and 0.0460 for $N = 18$ pH_2.

[1] C. Schran, F. Uhl, J. Behler, and D. Marx, J. Chem. Phys. **148**, 102310 (2018).

[2] F. Brieuc, C. Schran, F. Uhl, H. Forbert, and D. Marx, J. Chem. Phys. **152**, 210901 (2020).

[3] J. Čížek, J. Chem. Phys. **45**, 4256 (1966).

[4] R. J. Bartlett, J. Phys. Chem. **93**, 1697 (1989).

[5] R. J. Bartlett and M. Musial, Rev. Mod. Phys. **79**, 291 (2007).

[6] T. B. Adler, G. Knizia, and H. J. Werner, J. Chem. Phys. **127**, 221106 (2007).

[7] G. Knizia, T. B. Adler, and H.-J. Werner, J. Chem. Phys. **130**, 054104 (2009).

[8] R. A. Kendall, T. H. Dunning, and R. J. Harrison, J. Chem. Phys. **96**, 6796 (1992).

[9] D. E. Woon and T. H. Dunning, J. Chem. Phys. **100**, 2975 (1994).

[10] S. F. Boys and F. Bernardi, Mol. Phys. **19**, 553 (1970).

[11] H. J. Werner, P. J. Knowles, G. Knizia, F. R. Manby, and M. Schütz, Wiley Interdiscip. Rev. Comput. Mol. Sci. **2**, 242 (2012).

[12] H.-J. Werner, P. J. Knowles, F. R. Manby, J. A. Black, K. Doll, A. Heßelmann, D. Kats, A. Köhn, T. Korona, D. A. Kreplin, Q. Ma, T. F. Miller, A. Mitrushchenkov, K. A. Peterson, I. Polyak, G. Rauhut, and M. Sibaev, J. Chem. Phys. **152**, 144107 (2020).

[13] I. F. Silvera and V. V. Goldman, J. Chem. Phys. **69**, 4209 (1978).

[14] T. Zeng, H. Li, R. J. Le Roy, and P.-N. Roy, J. Chem. Phys. **135**, 094304 (2011).